

# Numerical study of strong shear nonequilibrium phenomenon and its relaxation mechanism in hypersonic Knudsen layer flows based on the direct simulation Monte Carlo method

Liu wenbin (✉ [ahwoahwo@163.com](mailto:ahwoahwo@163.com))

Beihang University

Wenbin Liu

Beihang University

Zhang Jinbai

Beihang University

Lee Chun-Hian

Beihang University

---

## Research Article

**Keywords:** Hypersonic flow, Rarefied aerodynamics, Knudsen layer, Nonequilibrium relaxation, DSMC

**Posted Date:** May 25th, 2022

**DOI:** <https://doi.org/10.21203/rs.3.rs-1656543/v1>

**License:**   This work is licensed under a Creative Commons Attribution 4.0 International License.

[Read Full License](#)

---

# Abstract

Based on the different flowfield and wall settings, a series of plane Couette flows of rarefied argon gas are simulated by the direct simulation Monte Carlo method, and the relaxation process of shear nonequilibrium has been systematically analyzed. The statistical result of molecular streamwise velocity ( $v_x$ ) shows a qualitatively platform-shaped distribution under the conditions of diffuse-reflection wall, low wall temperature, small wall spacing (roughly within the range of Knudsen layer), and large wall speed and shear rate. The simplified mechanism of this platform-like phenomenon is deduced, which proves that after the collision between two molecules reflected from the different walls (named the dual-wall molecular collision), their  $v_x$  will be uniformly distributed. Thus, if all reflected molecules occur once dual-wall molecular collision on average, their  $v_x$  will form the platform-shaped distribution. This conclusion is demonstrated by the verification cases. Similar phenomena can be found in more general flows, such as the hypersonic flow over a flat plate. The nonequilibrium phenomenon in the flat-plate flow can be explained by the equivalent relaxation process of dual-wall molecular collision, which indicates that the platform-like phenomenon is a universal nonequilibrium state in strong-shear rarefied flow, and they share a similar relaxation mechanism. The analysis of this phenomenon will help us to understand and model the relaxation process of hypersonic Knudsen layer flow.

## 1 Introduction

Experiments conducted by Smoluchowski [1] and Knudsen [2] revealed some nonequilibrium phenomena (e.g., velocity slip and temperature jump) in the near-wall flow. These phenomena usually appear within the range of several mean free paths ( $\lambda$ ) above the wall [3], and this rarefied gas region is traditionally called the Knudsen layer. Many physical problems involve the rarefied flow within the Knudsen layer, e.g., vaporization [4, 5], adsorption/desorption [6, 7], ablation [8, 9], and micro/nano flows concerning slip effect and momentum/energy transfer between gas and solid [10–14]. Considering that the aerodynamic/aerothermal prediction of hypersonic vehicle depends on the gas-solid momentum/energy transfer, some works have been made to study the hypersonic Knudsen layer flow [14–19]. Gijare, Bhagat, and Dongari [14, 15] studied the effect of the Knudsen layer on hypersonic flows using a computational fluid dynamics (CFD) solver modified based on the effective mean free path. Chrusciel and Pool [16] investigated the velocity slip and temperature jump in hypersonic Knudsen layer flow over the blunt body. Ou and Chen [17] investigated the nonlinear transport properties and macroscopic quantities of rarefied Couette flows at different velocities and found that transport properties are sensitive to the grid size. Chen and Zhou [18] analyzed several hypersonic flows over sharp bodies and blunt bodies and showed some special phenomena of velocity distributions in strong shear Couette flow. Darbandi and Roohi [19] applied a hybrid direct simulation Monte Carlo (DSMC)/Navier-Stokes approach to the hypersonic flows over nano flat plate and microcylinder cases. Akhlaghi and Roohi [20] found that the Knudsen layer thickness decreases with the increase of Mach number.

The strong shear exists near the surface of the hypersonic vehicle, which is extremely nonequilibrium in itself, and this additional nonequilibrium factor makes the Knudsen layer flow more complicated.

Therefore, in order to deeply understand the strong shear Knudsen layer flow, the key is to know well about its nonequilibrium relaxation process. From the microscopic point of view, the nonequilibrium relaxation is a process in which the nonequilibrium-distributed molecules transfer and convert their momentum and energy by incessantly interacting with other molecules (i.e., the molecular collision in the kinetic theory of gases) so that their velocity distribution approaches the equilibrium state. The change of flow state is mainly determined by the frequency and times of collisions, i.e., the higher the collision frequency is, the faster the relaxation rate is; the more the number of collisions is, the closer the flow approaches the equilibrium state.  $\lambda$  is the average molecular displacement between two successive collisions,  $|1/\lambda|$  reflects the collision frequency in terms of space, so  $\lambda$  is often used as a reference length to measure the characteristics of rarefied flow. Theoretically, the change of flow state with relaxation distance should be closely related to the spatial collision frequency. However, the effects of rarefaction and nonequilibrium have decisive influences on  $\lambda$ , and the change rule of  $\lambda$  in the Knudsen layer is a priority problem to be studied before employing  $\lambda$  to analyze the relaxation process [21–23]. To et al. [21] found a reduction of  $\lambda$  near the wall due to the boundary limiting effect. Whitman et al. [22] simulated the flow with a density gradient and found the directional dependence of  $\lambda$ . Dongari et al. [23] simulated the flows with different gas densities and wall confinements based on the L-J potential and calculated  $\lambda$  according to the hard-sphere (HS) collision in these flows and proposed a power-law distribution of molecular free path. Because the collision is a simplification of molecular interaction,  $\lambda$  is usually estimated based on the particle collision model, e.g., the HS model or variable-hard/soft-sphere (VHS/VSS) model. Different models inevitably have discrepancies in estimating the value of  $\lambda$ . In addition,  $\lambda$  will change dramatically with other flow parameters in the strong shear flow. In this case,  $\lambda$  needs to be corrected based on the numerical simulation results [18]. Furthermore, according to the computational experience in numerical simulation, there is always grid sensitivity when calculating the flow parameters in extremely nonequilibrium flow [17], and  $\lambda$  is no exception. Therefore, it may bring some uncertainty into the analysis of nonequilibrium relaxation based on the traditionally defined  $\lambda$  [24]. Although the reference length will not directly affect the physical process, a reasonable reference length with more explicit physical meaning that can reflect the influence of the nonequilibrium factor will be helpful for the analysis of Knudsen layer flow. An alternative thought is to find a characteristic length corresponding to the specific relaxation phenomenon and spatial collision frequency by observing the nonequilibrium relaxation process. The present work has carried out some exploration around this thought.

Many numerical and theoretical methods can provide the macroscopic information of Knudsen layer flow, e.g., methods of the kinetic theory of gases [25, 26], conventional CFD method [27, 28], DSMC method [29, 30], molecular dynamics (MD) method [21, 31], and other derivative methods [19, 32]. DSMC and MD can reveal the variations of molecular velocity distribution because they directly simulate molecular motion. Hence, they are feasible tools to study the nonequilibrium relaxation in Knudsen layer flow. In view of the relatively large computational consumption of MD, most flow cases are simulated by DSMC in this study.

The remainder of this paper is organized as follows: In Sec. 2, the DSMC settings of the plane Couette flow of rarefied argon gas is outlined, the effect of flowfield settings on flow is parametrically studied, and

a specific relaxation phenomenon is found. In Sec. 3, in light of some idealized assumptions, the simplified mechanism of such a phenomenon is deduced and verified, and then the significance is discussed. In Sec. 4, the above results and discussions are extended to explain the relaxation phenomenon in a more general flow. The conclusions are provided in Sec. 5.

## 2 Parametric Study On Strong Shear Knudsen Layer Flow

### 2.1 Physical model and DSMC settings

In this study, the plane Couette flow of rarefied argon gas was employed to model the Knudsen layer flow because it has a translation-invariant property, that is, its streamwise velocity will remain constant along the direction parallel to the wall, and flow parameters only change along the direction perpendicular to the wall (i.e., the shear gradient direction). Based on this flow, it is easy to observe the developments of nonequilibrium phenomena along the shear gradient direction. The argon gas was chosen because of its chemical stability to simplify simulation and analysis.

In order to provide a benchmark for the parametric study, a test case of plane Couette flow was simulated by the DSMC code based on the algorithm of Bird. The DSMC code has been tested and detailed in our previous articles [33, 34]. Figure 1 shows the physical model and simulation result of the test case. The contour of the translational velocity of flow ( $u_x$ ) keeps unchanged along the  $x$  direction, and the  $u_x$  profile varies linearly along the  $z$  direction. Therefore, such a simple flow is a suitable model to investigate the nonequilibrium relaxation process under strong shear.

The settings in the test case are as follows: the argon gas is driven by the upper wall along the positive  $x$  direction at the velocity value  $u_{up}$ ; the lower wall is fixed at coordinate  $z = 0$ , i.e., the lower-wall speed is 0; the spacing between the two walls is  $L_z$ ; the reference shear rate  $\gamma = u_{up}/L_z$ ; the length of the wall is  $L_x$ ; the wall model is the CLL model; the molecules are diffusely reflected on the wall, i.e., the CLL model's accommodation coefficient  $\alpha = 1$  (both the tangential and normal accommodation coefficients are collectively denoted as  $\alpha$  and set to the same value); the boundaries of gas are periodic. Thus, this case was simulated based on the canonic ensemble (i.e., the NVT ensemble). The initial conditions of this flow are as follows: the initial temperatures of the gas ( $T_0$ ) and walls ( $T_w$ ) are 300 K; the overall molecular number density  $n_0 = 1.333 \times 10^{20} \text{ m}^{-3}$ ; the initial speed of sound  $a_0 = 322.6 \text{ m/s}$ ;  $u_{up} = 4840 \text{ m/s}$  (i.e., the Mach number  $Ma = u_{up}/a_0 = 15$ ); the initial mean free path  $\lambda_0 = 10 \text{ mm}$ , here,  $\lambda_0$  is estimated by the variable-hard-sphere (VHS) collision model [35], i.e.,  $\lambda_T = [2^{1/2}\pi d_{ref}^2 n_0 (T_{ref}/T_0)^{\omega-0.5}]^{-1}$ , where  $d_{ref}$  ( $= 4.17 \text{ \AA}$ ) is the reference molecular diameter of argon at the reference temperature  $T_{ref}$  ( $= 273 \text{ K}$ ), and the argon viscosity index  $\omega = 0.81$  [36];  $L_x = 20\lambda_0 = 200 \text{ mm}$ ;  $L_z = 6\lambda_0 = 60 \text{ mm}$  (i.e., the Knudsen number  $Kn = \lambda_0/L_z = 1/6$ ). To facilitate the display of flowfield settings, we chose  $a_0$  and  $\lambda_0$  as reference quantities to measure and nondimensionalize the velocity and length quantities, respectively. In order to more carefully examine the change of flow under strong shear, the flowfield was divided into rectangular cells, and all cell sizes were refined to be  $0.1\lambda_0$  ( $= 1 \text{ mm}$ ), so the number of cells is  $200 \times 60$  ( $x \times z$ ). The mean number

of virtual molecules per cell is 20, and the total number of simulated virtual molecules is  $2.4 \times 10^5$ . The time step ( $\Delta t$ ) is  $2 \times 10^{-7}$  s. The initial molecular velocity ( $v_0$ ) is given by  $z_0 \gamma i + v_T$ , where  $z_0$  is the initial  $z$  coordinate of the molecule,  $i$  is the unit vector in the  $x$  direction, and  $v_T$  is the thermal velocity of molecules based on  $T_w$ . The  $10^5 \Delta t$  of initialization was performed at first, and then the simulation results were sampled and recorded every  $20 \Delta t$ .

## 2.2 Molecular velocity distributions of test case

The detail of nonequilibrium relaxation is hard to show from the perspective of macroscopic quantities, but the distribution variation of molecular velocity ( $v$ ) can reveal more information about the relaxation process. Therefore, by observing the variations of the  $v$  distribution and its moment function, we try to provide some reference and guidance for the subsequent parametric study of the relaxation phenomena in Sec. 2.3.

In order to investigate the change of  $v$  distribution along the  $z$  direction, all cells with the same  $z$  coordinate are regarded as the statistical region of the same layer. The flowfield was divided into 60 statistical layers with a spacing of  $\Delta z = 0.1 \lambda_0$ . For a layer with such a small spacing, the variation of  $v$  distribution in one layer can be ignored.

Figure 2 shows the variations of  $N_v/N_{\text{total}}$  [where  $N_v$  is the molecular number in a certain velocity interval (spacing is  $\Delta v = 40$  m/s) in a layer, and  $N_{\text{total}}$  is the total molecular number counted in this layer] with  $v_x$ ,  $v_y$ , and  $v_z$  (nondimensionalized by  $a_0$ ) in five representative statistical layers (i.e., layers  $z = 0.1 \lambda_0$ ,  $1.5 \lambda_0$ ,  $3 \lambda_0$ ,  $4.6 \lambda_0$ , and  $6 \lambda_0$ , where the layer is represented by its  $z$  coordinate of upper interface). For a certain velocity component  $v$ , the value of  $N_v/N_{\text{total}}$  is just the probability of molecules with this  $v$  among all molecules in a layer. Thus, the  $N_v/N_{\text{total}}$  curve corresponds to the  $v$  distribution in terms of probability. The variations of  $N_v/N_{\text{total}}$  curves intuitively reflect the relaxation process of  $v$  distributions.

Figure 2 shows a correlative symmetry between geometry and kinematics in Couette flow, i.e., for any two layers symmetrical about the central plane in space, their  $v$  distributions must be mirror symmetrical to each other. For example, as shown in Fig. 2(a), although the  $v_x$  distribution in layers  $z = 0.1 \lambda_0$  itself is asymmetrical, it is mirror symmetrical to that in layer  $z = 6 \lambda_0$  about  $v_x/a_0 = 7.5$ . At the central plane,  $v$  distribution itself is mirror symmetric. Because layer  $z = 3 \lambda_0$  is adjacent to the central plane, and its  $v$  distributions (see green short dashed lines in Fig. 2) are almost symmetrical,  $v$  distributions in this layer can represent those at the central plane.

Figure 2(a) shows two peaks of  $v_x$  distribution at abscissas  $v_x/a_0 = 0$  and 15 in layers  $z = 0.1 \lambda_0$  and  $6 \lambda_0$ , which just correspond to the wall speeds. These peaks are mainly formed by the molecules reflected from the wall (abbreviated as reflected molecules) with small thermal velocity ( $v_T$ ). Thus, as shown in Fig. 2, the velocities of reflected molecules are concentrated near the wall speeds. That is, the  $v$  distribution of reflected molecules contains the velocity information of the wall (e.g., translational and thermal velocities), and this peak-like distribution is intuitively described as the reflected molecular peak. However,

it should be pointed out that this description is not a strict definition. The molecules counted in the reflected molecular peak also include a few molecules that have been relaxed to a certain extent in the bulk flow (abbreviated as relaxed molecules), so the reflected molecular peak does not strictly follow the velocity information of wall-diffuse-reflection. The existence of relaxed molecules is represented by the widely distributed  $v_x$  between the two peaks in Fig. 2(a), which indicates that these molecules have an average velocity visibly deviated from the wall speed and a large thermal velocity. This is consistent with the general understanding of strong shear flow, i.e., the bulk flow is heated by the viscous dissipation of shear relaxation, so the distribution of relaxed molecules manifests the velocity information of bulk flow. As the  $z$  coordinate increases (or decreases), the reflected molecular peak at  $v_x/a_0 = 0$  (or 15) is gradually reduced, and the relaxed molecules increase continuously until a platform-like transition forms near the central plane (i.e., layer  $z = 3\lambda_0$ ).

This distinctive nonequilibrium phenomenon can also be found in similar cases of Ref. [18], and this feature of velocity distribution must be caused by the significant velocity change of reflected molecules due to collisions. However, the gas molecules reflected from the same wall (abbreviated as same-wall molecules) share the same  $v$  distribution. According to the conservation of momentum, the collisions between the same-wall molecules will not make their  $v_x$  distribution deviate from the wall speed collectively. Thus, the same-wall molecular collision is not the main mechanism of shear relaxation. The  $v$  distribution of reflected molecules will change drastically only after colliding with other molecules based on different  $v_x$  distributions (e.g., relaxed molecules and reflected molecules from the opposite wall), and the reflected molecules turn into the relaxed molecules at this time. Therefore, qualitatively speaking, the root of the relaxation phenomenon in Fig. 2 is the non-same-wall molecular collision. Similar trends appear in the  $v_y$  and  $v_z$  distributions [see Figs. 2(b, c)], i.e., the  $v_y$  (or  $v_z$ ) distribution peak of reflected molecules is cut down by collisions and converted into a more dispersed and symmetric distribution near the central plane.

The variation of the statistical moment functions [e.g., variance  $\sigma(v)$ , skewness  $S(v)$ , and kurtosis  $K(v)$ ] of  $v$  distribution along the  $z$  direction will help us to understand the relaxation process more comprehensively. Figure 3 shows the variations of  $\sigma(v)/\sigma_{\max}$  [where  $\sigma_{\max}$  is the maximum value of  $\sigma(v)$ ],  $S(v)$ , and  $K(v)$  with  $z/\lambda_0$ . The curves of moment functions reconfirm the correlative symmetry about the central plane: the even order moments  $\sigma(v)$  and  $K(v)$  are mirror symmetric; the odd order moment  $S(v)$  has rotational symmetry.  $\sigma(v)$  corresponds to the thermal velocity, and it can be known that thermal motion near the central plane is the most intense. Because  $S(v)$  represents the asymmetry of  $v$  distribution, and the  $v_y$  distribution [see Fig. 2(b)] is almost symmetric,  $S(v_y)$  is basically 0 [see blue dotted line in Fig. 3(b)].

As shown in Fig. 3, the moment function curves of all components of  $v$  near the central plane have the features of  $\sigma_{\max}$ , zero-value  $S(v)$  (denoted as  $S_0$ ), and minimum  $K(v)$  (denoted as  $K_{\min}$ ). As shown in Fig. 2,  $v$  distributions in layer  $z = 3\lambda_0$  deviate from the equilibrium seriously. We thus guess that these specific moment function values ( $\sigma_{\max}$ ,  $S_0$ , and  $K_{\min}$ ) may be typical features of the extreme nonequilibrium in strong shear Couette flow. In addition,  $v_x$  distribution changes most dramatically and

has the most distinctive nonequilibrium phenomenon. Thus,  $v_x$  is the representative velocity component in Couette flow and is selected to be the main research object in this investigation. This specific relaxation state of  $v_x$  distribution is also reflected in the moment function value, i.e., the minimum  $K(v_x)$  is 1.81 [see red dashed line in Fig. 3(c)], which is very close to the  $K(v)$  ( $= 1.8$ ) of uniform distribution. The minimum  $K(v_x)$  is obviously different from the minimums  $K(v_y)$  ( $= 3.06$ ) and  $K(v_z)$  ( $= 3.43$ ), which are relatively close to the  $K(v)$  ( $= 3$ ) of equilibrium distribution. Therefore,  $K_{\min}$  can be used as the indicator to identify the specific relaxation state of  $v_x$  distribution.

## 2.3 Parametric study based on different settings of flowfield

The plane Couette flow is symmetrical, but a general flow may not have symmetry. We thus try to decouple the role of a single wall in the relaxation process of Couette flow and provide some references for the study of more general flows.

Because the original information of a single wall is carried by the molecules reflected from this wall, and the motion of reflected molecules along  $z$  direction is unidirectional (i.e., either  $v_z > 0$  or  $v_z < 0$ ), the spreading of wall velocity information is also directional. Therefore, the  $v$  distribution in the global velocity space can be regarded as the superposition of the  $v$  distributions based on two opposite velocity half-spaces (i.e.,  $v_z > 0$  and  $v_z < 0$ ). Figures 2 and 3 indicate that the global-space distribution of Couette flow has correlative symmetry between geometry and kinematics. In order to ensure this correlative symmetry, either each half-space distribution itself is correlative symmetrical, or they are correlatively symmetrical to each other. For example, the  $v_x$  distribution of layer  $z = 0.1\lambda_0$  based on  $v_z > 0$  is mirror symmetrical to that of layer  $z = 6\lambda_0$  based on  $v_z < 0$ . If these two half-space distributions are correlatively symmetrical to each other, as long as one distribution is known, the other can be determined accordingly. In this case, the influence of the single wall can be decoupled to some extent, and the relaxation process can be analyzed by observing the change of  $v$  distribution based on a unidirectional velocity half-space. This assumption can be confirmed to be self-consistent in the following discussion. We thus attempted to analyze the role of the lower wall by studying the variation of the  $v_x$  distribution based on the upward velocity half-space (i.e.,  $v_z > 0$ ). In this section, unless otherwise specified, the  $v_x$  distribution only refers to the half-space  $v_x$  distribution based on  $v_z > 0$ .

In this section, the effects of the flowfield settings (e.g., wall spacing  $L_z$ , wall speed  $u_{up}$ , and shear rate  $\gamma$ ) and wall settings (e.g., wall temperature  $T_w$  and accommodation coefficient  $\alpha$ ) on the nonequilibrium relaxation are studied parametrically, and five groups of Couette flows were simulated.

### 2.3.1 Group 1 with fixed $L_z$

In group 1,  $L_z$  is fixed, and  $\gamma$  varies with  $u_{up}$  accordingly. The settings in group 1 are given in Table 1:  $L_z$  and  $u_{up}$  are nondimensionalized by  $\lambda_0$  and  $a_0$ , respectively;  $\gamma$  is nondimensionalized by  $\lambda_0$  and  $a_0$ , i.e.,  $\gamma\lambda_0/a_0$ , which describes the shear nonequilibrium effect [18, 37]. Other settings remain the same as Sec. II.A.

Table 1  
Settings of group 1.

Group 1	$L_z/\lambda_0$	$u_{up}/a_0$	$\gamma\lambda_0/a_0$	$T_w(K)$	$\alpha$
Case 1.1	6	0	0.000	300	1
Case 1.2	6	3	0.500	300	1
Case 1.3	6	6	1.000	300	1
Case 1.4	6	9	1.500	300	1
Case 1.5	6	12	2.000	300	1
Case 1.6	6	15	2.500	300	1

Figure 4 shows the variations of  $\sigma(v_x)$ ,  $S(v_x)$ , and  $K(v_x)$  of group 1 along the  $z$  direction. The flow of case 1.1 is in equilibrium, so the values of  $\sigma(v_x)/\sigma_{max}$ ,  $S(v_x)$ , and  $K(v_x)$  in case 1.1 (see blue solid lines in Fig. 4) are always equal to 1, 0, and 3, respectively. As  $u_{up}$  and  $\gamma\lambda_0/a_0$  increase, the moment-function curves of  $v_x$  distribution deviate gradually from those of case 1.1, meaning that the flow with stronger shear is more nonequilibrium. These asymmetric curves indicate that the half-space  $v_x$  distribution itself does not have correlative symmetry. Thus, the half-space  $v_x$  distribution based on  $v_z > 0$  should be correlatively symmetrical to that based on  $v_z < 0$ , and it is reasonable to take the half-space  $v_x$  distribution as a decoupled factor to study the relaxation process of strong shear Knudsen layer flow.

For all cases except case 1.1, the features ( $\sigma_{max}$ ,  $S_0$ , and  $K_{min}$ ) appear in very close positions, which somehow recurs the features in Fig. 3. However, the half-space distribution itself is not correlative symmetrical, so the layers with features ( $\sigma_{max}$ ,  $S_0$ , and  $K_{min}$ ) are not located at the central plane but concentrated between  $z = 4.2\lambda_0$  and  $4.4\lambda_0$ . Figure 4(c) shows that the value of  $K_{min}$  varies from 2.83 (case 1.2) to 2.03 (case 1.6).  $K_{min}$  of case 1.6 is relatively close to  $K(v)$  of uniform distribution, which suggests that the platform-like phenomenon may also occur in the half-space  $v_x$  distribution. Considering the significance of  $K_{min}$  mentioned previously, we thus trace the layer characterized by  $K_{min}$  (denoted as the  $K_{min}$  layer) to observe the evolution of the nonequilibrium relaxation process. The distance from the lower wall to the position where the  $v_x$  distribution featured with  $K_{min}$  is denoted as  $L_{Km}$ .

Figure 5 shows the variations of  $v_x$  distributions in several representative layers in the results of group 1, and blue dotted lines represent the results of the  $K_{min}$  layers. Figure 5(a) shows that the  $v_x$  distributions in case 1.1 remain the same Maxwellian distribution, because this flow is in equilibrium. Figures 5(b-f) also

show the peaks of  $v_x$  distribution at corresponding wall speeds in layers  $z = 0.1\lambda_0$  and  $6\lambda_0$  in different cases. However, the peak in layers  $z = 6\lambda_0$  is not an upper-wall reflected molecular peak, because the  $v_z$  of molecules reflected from the upper wall is minus. This peak is formed by the molecules that carry the velocity information of upper wall after collisions. Because the moment curves of case 1.2 are close to those of case 1.1 (see Fig. 4), the  $v_x$  distributions in case 1.2 approximate the quasi-equilibrium distribution [see Fig. 5(b)], which indicates that the flow is almost fully relaxed when  $u_{up}$  and  $\gamma$  are small. As  $u_{up}$  and  $\gamma$  increase, the flow deviates from the quasi-equilibrium, and the  $v_x$  distribution in the  $K_{min}$  layer gradually transforms into a platform-shaped distribution [see Fig. 5(f)]. Hence, the platform-like phenomenon does reflect the specific relaxation state under strong shear.

As discussed above, at the central plane, the half-space  $v_x$  distribution based on  $v_z > 0$  should be correlatively symmetrical to that based on  $v_z < 0$ . As shown in Fig. 5(f), for the  $v_x$  distribution at the central plane based on  $v_z > 0$ , its  $N_v/N_{total}$  decreases almost linearly with  $v_x/a_0$ . Accordingly, the corresponding  $N_v/N_{total}$  based on  $v_z < 0$  should increase linearly. Thus, the superposition of these two half-space  $v_x$  distributions forms the platform-like transition of global-space  $v_x$  distribution in Figs. 2(a). Although the direct causes of such platform-like phenomena in Figs. 2(a) and 5(f) are different, they may share the same root of physical mechanism, which will be discussed in Sec. III.

## 2.3.2 Group 2 with fixed $u_{up}$

In group 2,  $u_{up}$  is fixed, and  $\gamma$  decreases with the increase of  $L_z$ . The settings in group 2 are given in Table II. The mean number of virtual molecules per cell and the cell size keep unchanged, so the numbers of cell and virtual molecules should increase with  $L_z$  accordingly.

Table 2  
Settings of group 2.

Group 2	$L_z/\lambda_0$	$u_{up}/a_0$	$\gamma\lambda_0/a_0$	$T_w(K)$	$\alpha$
Case 2.1	2	15	7.500	300	1
Case 2.2	4	15	3.750	300	1
Case 2.3	6	15	2.500	300	1
Case 2.4	8	15	1.875	300	1
Case 2.5	10	15	1.500	300	1
Case 2.6	12	15	1.250	300	1

Figure 6 shows the variations of  $v_x$  distributions in group 2. Figure 6(a) shows that when  $z \geq 1.7\lambda_0$ , the  $v_x$  distribution in case 2.1 presents a bimodal structure with a platform-like transition. In other words, the lower-wall reflected molecular peak (at  $v_x/a_0 = 0$ ) is not eliminated during the relaxation process. Or qualitatively, within such a short relaxation distance ( $2\lambda_0$ ), there are too few intermolecular collisions to

fully relax the wall velocity information carried by lower-wall reflected molecules. As shown in Figs. 6(a-c), all cases with  $L_z \leq 6\lambda_0$  have obvious platform-like phenomena, which suggests that the physical mechanism leading to the platform-like phenomenon plays an important role in a relatively short relaxation distance. Generally, as  $L_z$  and relaxation distance increase, the molecules carrying wall velocity information will experience more collisions during the spread and relaxation process. Due to the further relaxation caused by the increase of collision, the  $v_x$  distribution of the  $K_{\min}$  layer gradually transforms from the platform-like distribution into an ordinary unimodal structure [see Figs. 6(d-f)], the value of  $K_{\min}$  increases from 1.56 (case 2.1) to 2.46 (case 2.6). In other words, the platform-like phenomenon will not appear if  $\gamma$  is small.

### 2.3.3 Group 3 with fixed $\gamma$

In group 3,  $\gamma$  is fixed, and  $u_{\text{up}}$  varies with  $L_z$  accordingly. The settings in group 3 are given in Table III.

Table 3  
Settings of group 3.

Group 3	$L_z/\lambda_0$	$u_{\text{up}}/a_0$	$\gamma\lambda_0/a_0$	$T_w(\text{K})$	$\alpha$
Case 3.1	2	5	2.500	300	1
Case 3.2	4	10	2.500	300	1
Case 3.3	6	15	2.500	300	1

Figure 7 show that there is always a platform-like phenomenon in the  $K_{\min}$  layer in any case of group 3, and their values of  $K_{\min}$  vary slightly from 1.98 (case 3.1) to 2.03 (case 3.3). This shows that although  $u_{\text{up}}$  in case 3.1 is relatively small, the physical root of the platform-like phenomenon still works as long as  $\gamma$  is large enough.

Figure 7 shows that  $L_{K_{\min}}$  increases from  $1.7\lambda_0$  (case 3.1) to  $4.4\lambda_0$  (case 3.3), which is consistent with the trend of the overall  $\lambda$  ( $\lambda_{\text{all}}$ ) in the entire flowfield. Generally, the average temperature of entire flowfield is positively correlated with the overall energy of system determined by  $u_{\text{up}}$ , and  $\lambda$  is positively correlated with temperature, so  $\lambda_{\text{all}}$  increases with  $u_{\text{up}}$  from  $1.5\lambda_0$  (case 3.1) to  $2.8\lambda_0$  (case 3.3), and the distance of reflected molecules relaxing to a specific relaxation state (e.g., the platform-shaped distribution) should also increase. In addition,  $L_{K_{\min}}/\lambda_{\text{all}}$  is less than 2, meaning that platform-like phenomena just appear in the region traditionally regarded as the Knudsen layer ( $1\lambda$  to  $2\lambda$ ). This also implies that within the relaxation distance of  $L_{K_{\min}}$ , the orders of magnitude of the number of collisions are very close in all cases of group 3. Therefore, the wall velocity information may have experienced a somehow equivalent relaxation process before reaching the specific relaxation state (i.e., the platform-shaped distribution), and the average number of collisions during this equivalent relaxation process may have the same order of magnitude.

According to the results of Secs. II.C.1 to II.C.3, the platform-like phenomenon occurs in the flowfield with a short relaxation distance and large shear rate.

## 2.3.4 Group 4 with different $T_w$

Because case 1.6 has a typical platform-shaped distribution, it is taken as a benchmark (i.e., case 4.1) to analyze the influence of  $T_w$ . The settings in group 4 are given in Table IV, and only  $T_w$  is variable.

Table 4  
Settings of group 4.

Group 4	$L_z/\lambda_0$	$u_{up}/a_0$	$\gamma\lambda_0/a_0$	$T_w(K)$	$\alpha$
Case 4.1	6	15	2.500	300	1
Case 4.2	6	15	2.500	600	1
Case 4.3	6	15	2.500	900	1

Figure 8 shows that all cases have platform-like phenomena, the  $v_x$  distribution is more dispersed at a higher  $T_w$ , and the  $K_{min}$  varies slightly from 2.03 (case 4.1) to 2.11 (case 4.3). It can be seen that the effect of  $T_w$  is not significant, i.e., as long as the distribution of thermal velocity is not too dispersed and covers the velocity difference between the two walls, the platform-like phenomenon still appears. The smaller  $T_w$  is, the more typical the platform-like phenomenon is.

## 2.3.5 Group 5 with different $\alpha$

The accommodation coefficient  $\alpha$  of the CLL model is related to the molecular interaction and energy exchange between gas and solid. When  $\alpha = 1$ , gas molecules are diffusely reflected on the wall, and their energy is completely transferred to the wall; when  $\alpha = 0$ , gas molecules are specularly reflected by the wall, and they do not exchange energy with the wall at all. Therefore, the cases of group 5 are simulated to investigate the influence of the physical property of the wall on the relaxation process. Based on different wall materials, the accommodation coefficient varies from 0.1 to 0.95 [38–41], so six values of  $\alpha$  are given in Table IV.

Table 5  
Settings of group 5.

Group 5	$L_z/\lambda_0$	$u_{up}/a_0$	$\gamma\lambda_0/a_0$	$T_w(K)$	$\alpha$
Case 5.1	6	15	2.500	300	1/6
Case 5.2	6	15	2.500	300	2/6
Case 5.3	6	15	2.500	300	3/6
Case 5.4	6	15	2.500	300	4/6
Case 5.5	6	15	2.500	300	5/6
Case 5.6	6	15	2.500	300	6/6

Figure 9 shows the variations of  $v_x$  distributions in group 5. Figure 9(a) shows that the  $v_x$  distributions in case 5.1 approximate the quasi-equilibrium distribution. This is because when  $\alpha = 1/6$ , the reflection on the wall is close to specular reflection. If gas molecules are specularly reflected, the wall will not transfer any information to the gas, and the flow will be fully relaxed into an equilibrium flow. If the reflection deviates slightly from the specular reflection, its  $v_x$  distribution will become a quasi-equilibrium distribution, just like case 5.1 shown in Fig. 9(a). As  $\alpha$  increases, the flow deviates more and more from equilibrium flow until the platform-like phenomenon appears in the case based on diffuse reflection.

## 3 Mechanism Analysis

### 3.1 Theoretical derivation

The results in Sec. II show that during the relaxation process of strong shear Couette flow, the  $v_x$  distribution always evolves into an extreme nonequilibrium distribution with moments ( $\sigma_{max}$ ,  $S_0$ , and  $K_{min}$ ) in the  $K_{min}$  layer. Furthermore, under the conditions of small  $L_z$ , large  $u_{up}$  (or  $\gamma$ ), low  $T_w$ , and diffuse-reflection wall, the  $K_{min}$  layer will present a specific relaxation state of platform-shaped distribution. As discussed in Sec. II.B, the root of the platform-like phenomenon is qualitatively attributed to the non-same-wall molecular collision. This section will further deduce and analyze the physical mechanism of this phenomenon.

Extending the above conditions of the platform-like phenomenon to extreme situations (e.g., an very rarefied and strong shear flow with a tiny  $T_w$ ) and ignoring some secondary factors will help us to analyze the physical mechanism of platform-like phenomenon. According to  $Kn = \lambda_0/L_z$ , if  $\lambda$  remains unchanged, the smaller  $L_z$  is, the greater  $Kn$  is, and the flow is more rarefied. According to  $\gamma = u_{up}/L_z$ , if  $u_{up}$  remains unchanged, the smaller  $L_z$  is, the greater  $\gamma$  is, and the shear is stronger. Thus, to model the extremely rarefied and strong shear flow requires a very short spacing of walls (i.e.,  $L_z$ ). However,  $L_z$  should not be too small. Considering that the velocity of gas molecules will be reset randomly when they

hit on and are diffusely reflected from the wall, the molecular movement process between two successive collisions can be regarded as an independent motion period. Qualitatively speaking, for a molecule at any velocity, the smaller the  $L_z$  is, the sooner it moves to hit the wall again (i.e., the shorter the motion period is), and the probability and number of potential collisions during this period are reduced accordingly. In extreme cases, when  $L_z$  reduces to some extent (e.g.,  $Kn > 10$ ), the flow becomes a free molecule flow. In this flow, collision, momentum transfer, energy dissipation, and nonequilibrium relaxation phenomenon will not occur, which makes the relaxation process meaningless. Therefore, molecular collisions (especially non-same-wall molecular collisions) are necessary to reproduce the relaxation process and nonequilibrium phenomenon under strong shear. Based on the above discussion, we assume that a gas molecule only experiences non-same-wall molecular collision once at most in a motion period. Considering the correlation between the number of collisions and  $L_z$ , this hypothetical flowfield naturally has a small wall spacing.

The molecules of non-same-wall molecular collisions may be relaxed molecules or reflected molecules from the opposite wall. Since a molecule in this hypothetical flow only experiences non-same-wall molecular collision once in a motion period, it will not collide again after it turns into the relaxed molecule by collision. In this case, the two molecules of the non-same-wall collision must be reflected from different walls, and such a collision is abbreviated as the dual-wall molecular collision. Thus, the following discussion sets that the target molecule A is reflected from the lower wall, and the test molecule B is reflected from the upper wall.

The relative velocity ( $c_r$ ) of dual-wall molecular collision is generally very high in this investigation. According to the variable-hard-sphere model, the collision cross-section [ $\sigma_T(c_r)$ ] is proportional to  $c_r^{1-2\omega}$  ( $= c_r^{-0.62}$ , where  $\omega = 0.81$ ). Hence, with the increase of  $c_r$ , the change rate of  $\sigma_T(c_r)$  will decay, so the collision model is simplified to the ordinary hard-sphere collision in the following discussion.

Suppose the wall temperature ( $T_w$ ) is so small that the thermal velocity values of reflected molecules ( $v_T$ ) are almost negligible relative to  $u_{up}$ . However,  $T_w$  and  $v_T$  are tiny but should not be zero, because the diffusion of wall velocity information requires a  $z$ -direction thermal motion. Generally, the collision probability ( $P$ ) is positively correlated with  $c_r$ , i.e., within a  $\Delta t$ , the greater  $c_r$  is, the larger the space volume swept by the HS molecule is, and  $P$  is higher. Thus, for the two molecules in a same-wall molecular collision, their  $c_r$  is determined by  $v_T$ , so their  $c_r$  must be tiny, and their collision probability ( $P_{same}$ ) is negligible. However, for molecules A and B in a dual-wall molecular collision, their velocity values ( $v_A$  and  $v_B$ ) approach 0 and  $u_{up}$ , respectively, so their  $c_r \approx u_{up}$ , and their collision probability ( $P_{dual}$ ) cannot be ignored. Based on the above assumptions, in a hypothetical Couette flow where  $L_z$  is small enough and  $T_w$  is tiny but non-zero, the elementary process of the relaxation of strong shear nonequilibrium can be modelled as the collision of molecule B against molecule A at the relative velocity  $u_{up}$  (see Fig. 10).

The coordinate system in Fig. 10 is established at the centroid of molecule A, and the direction of  $u_{up}$  is the positive  $x$  direction.  $R$  is the radius of HS of molecule A. Molecule B collides with molecule A at the

collision point represented by the red dot. As shown in Fig. 10(a), the sharp angle between the  $x$ -axis and the radius passing through the collision point is defined as the collision angle ( $\theta$ ), where  $\theta \in [0, \pi/2]$ . All potential collision points whose  $\theta \in [\theta, \theta + d\theta]$  (where  $d\theta$  is an infinitesimal) form a ring belt on the sphere surface of molecule A (see the grey belt). Because only reflected molecules participate in this collision, and the reflected molecules A and B share the same thermal velocity and density, the collision will occur uniformly and randomly in space, i.e., the projection of collision point on the  $y$ - $z$  plane is uniformly distributed in the projected circle of the sphere of molecule A. Let  $F$  be the conditional probability under the condition that only such dual-wall molecular collisions are considered. For example, the probability of the collisions whose  $\theta \leq \theta_0$  can be denoted as  $F(\theta \leq \theta_0)$ . The conditional probability [ $dF$ , see Eq. (1)] whose  $\theta \in [\theta, \theta + d\theta]$  is the ratio of the projected area of the corresponding ring belt ( $dS = \pi R^2 \sin 2\theta d\theta$ ) to that of the sphere of molecule A ( $S = \pi R^2$ ). It is easy to prove that the integral of the right-hand term of Eq. (1) over the interval  $[0, \pi/2]$  is 1, i.e.,  $F(\theta \leq \pi/2) = 1$ .

$$dF = dS/S = 2\sin\theta\cos\theta d\theta. \quad (1)$$

As shown in Fig. 10(a), after the collision, molecule A bounces at  $v_A = v_n = u_{up}\cos\theta$  along the normal direction of sphere surface at the collision point, and molecule B bounces at  $v_B = v_t = u_{up}\sin\theta$  along the tangential direction. As shown in Fig. 10(b), the angle measured clockwise from the positive  $y$ -axis to the radius passing through the projection of the collision point is defined as the azimuth angle ( $\varphi$ ). The projections ( $v_{Az}$  and  $v_{Bz}$ ) of  $v_A$  and  $v_B$  on the  $z$ -axis are

$$v_{Az} = 0.5u_{up}\sin 2\theta\sin\varphi, \quad v_{Bz} = -0.5u_{up}\sin 2\theta\sin\varphi. \quad (2)$$

As previously assumed,  $v_T$  is much less than  $u_{up}$ , and then the component of  $v_T$  in the  $z$  direction ( $v_{Tz}$ ) is even tinier. According to Eq. (2), as long as  $\sin 2\theta\sin\varphi$  does not approach 0,  $v_{Az}$  and  $v_{Bz}$  are in the same order of magnitude as  $u_{up}$  and far greater than  $v_{Tz}$ . Because collision points are uniformly distributed in the projected circle, and the collision points satisfying  $\sin 2\theta\sin\varphi = 0$  are only distributed on the  $y$  axis and the edge line of the projected circle,  $v_{Az}$  and  $v_{Bz}$  are indeed much greater than  $v_{Tz}$  in most collisions. To summarize, for the reflected molecule in this hypothetical flow, either it has not experienced a dual-wall molecular collision and maintains a tiny  $v_{Tz}$ , or it turns into a relaxed molecule after such a collision and scatters at a much higher  $v_z$ . As long as  $L_z$  is small enough, the relaxed molecules with large  $v_z$  will pass through the flowfield and hit the wall in a short time without colliding again.

The projections ( $v_{Ax}$  and  $v_{Bx}$ ) of  $v_A$  and  $v_B$  on the  $x$ -axis are

$$v_{Ax} = u_{up}\cos^2\theta, \quad v_{Bx} = u_{up}\sin^2\theta. \quad (3)$$

It is clear that  $v_{Ax}$  and  $v_{Bx}$  are independent of  $\varphi$ . The total differentials of  $v_{Ax}$  and  $v_{Bx}$  are

$$dv_{Ax} = -2u_{up}\cos\theta\sin\theta d\theta, \quad dv_{Bx} = 2u_{up}\cos\theta\sin\theta d\theta. \quad (4)$$

Solving Eq. (1) and Eq. (4) simultaneously, we obtain

$$-dF/dv_{Ax} = dF/dv_{Bx} = 1/u_{up}. \quad (5)$$

Eq. (5) illustrates that when the random variable of the conditional probability is  $v_x$ , for the case where  $v_{Ax}$  (or  $v_{Bx}$ ) after the collision is any specific value, its absolute value of conditional probability density is always  $1/u_{up}$ . It should be noted that  $dF/dv_{Ax}$  ( $= -1/u_{up}$ ) is negative. According to Eq. (3), when  $\theta = 0$ , the dual-wall molecular collision is a central collision. After this collision, molecules A and B exchange their velocities, and  $v_{Ax}$  equals  $u_{up}$ . Thus, as  $\theta$  increases,  $v_{Ax}$  decreases, and  $dF/dv_{Ax}$  is negative. Because the derivations of Eqs. (3–5) are independent of  $\varphi$ , Eqs. (3–5) are always valid around  $x$  axis, and the  $v_x$  of molecule A (or B) is uniformly distributed in the range  $[0, u_{up}]$  after the collision. Therefore, the reflected molecules after dual-wall molecular collisions will form a uniform  $v_x$  distribution in the hypothetical flow.

## 3.2 Simulation verification

The deduction in Sec. III.A proves that for the hypothetical flow, if each reflected molecule only occurs one dual-wall molecular collision in one motion period, their  $v_x$  after collisions must be uniformly distributed. In real flow, besides the collisions of same-wall/dual-wall reflected molecules, there are re-collisions of relaxed molecules. According to the conclusion in Sec. III.A, the conditions of uniform distribution are that  $v_T$  is small and  $c_T$  is large. However, the  $v_T$  of relaxed molecules is large, and the  $c_T$  of same-wall molecules is small, so these non-dual-wall molecular collisions are not the root cause leading to the platform-shaped distribution. In order to verify this conclusion, the multipliers  $\beta \in [0, 1]$  are set to adjust the collision probability of different collision objects. When  $\beta = 0$ , the original probability of variable hard sphere model multiplied by  $\beta$  also equals 0, i.e., the collision will not happen. When  $\beta = 1$ , the original probability remains unchanged. The specific steps are as follows:

1. Mark the molecule reflected from the upper (or lower) wall as “+1 (or –1)”;
2. If a reflected molecule occurs a non-same-wall molecular collision, it becomes a relaxed molecule and marks “0”;
3. If the relaxed molecule hits on the wall and reflects again, its mark shall be reset to be “+1/–1”;
4. Set a multiplier  $\beta_0$  (or  $\beta_1$ ) to adjust the probability of re-collisions ( $P_{re}$ ) [or same-wall molecular collisions ( $P_{same}$ )].

For example, for a collision pair including two molecules, if the product of their marks is “–1”, meaning that the two molecules are reflected from different walls and have not experienced a dual-wall molecular collision. In this simulation,  $P_{dual}$  will not be adjusted because the dual-wall molecular collision is the physical root of shear nonequilibrium. After this collision, they are regarded as relaxed molecules, and their marks are changed to “0”. If the product of their marks is “0”, there must be at least one relaxed molecule in this collision pair, and this collision belongs to a re-collision. Now, multiple their  $P_{re}$  by  $\beta_0$ . Suppose the product of their marks equals “+1”, which means that the collision is a same-wall molecular

collision. Then, multiple their  $P_{\text{same}}$  by  $\beta_1$ . Within one  $\Delta t$ , the frequency of collisions is determined by  $P$ , so the total number of collisions ( $N_{\text{total}}$ ) can be scaled down by adjusting  $\beta$ , that is:

$$N_{\text{total}} = N_{\text{dual}} + \beta_0 N_{\text{re}} + \beta_1 N_{\text{same}}, \quad (6)$$

where  $N_{\text{dual}}$ ,  $N_{\text{re}}$ , and  $N_{\text{same}}$  are the numbers of dual-wall molecular collision, re-collision, and same-wall molecular collision, respectively. Thus,  $N_{\text{total}}$  increases with  $\beta$ , and the increase of  $N_{\text{total}}$  will result in further relaxation. Table 6 gives the settings of cases in group 6 with different  $\beta$ .

Table 6  
Settings of group 6.

Group 6	$L_z/\lambda_0$	$u_{\text{up}}/a_0$	$\gamma\lambda_0/a_0$	$T_w(\text{K})$	$\alpha$	$\beta_0$	$\beta_1$
Case 6.1	6	15	2.500	300	1	0.0	0.0
Case 6.2	6	15	2.500	300	1	1.0	0.0
Case 6.3	6	15	2.500	300	1	0.0	1.0
Case 6.4	6	15	2.500	300	1	1.0	1.0
Case 6.5	6	15	2.500	300	1	0.2	0.2
Case 6.6	6	15	2.500	300	1	0.5	0.5

Figure 11 shows the variation of flux  $v_x$  distributions in cases 6.1–6.4, where the flux  $v_x$  distribution records the  $v_x$  distribution in an upward molecular flux that is defined as all the molecules crossing the interface between two statistical layers along the positive  $z$  direction (i.e.,  $v_z > 0$ ). This statistical way was usually used in the study of gas-solid interaction [34] to observe the  $v$  distribution of incident/reflected molecular flux at the wall. Here, it is used to observe the  $v$  distribution after molecular collisions. For a certain molecule in a statistical layer, no matter how long it stays, how many times it collides, or how its velocity changes in this layer, it will only cross the adjacent upper interface at the velocity after its last collision, and only this velocity will be recorded in the flux distribution at this interface. Thus, the flux  $v_x$  distribution at a certain interface is just equivalent to the  $v_x$  distribution of the last collisions of molecules before passing through this interface. It should be noted that the  $v_x$  distribution mentioned in Sec. II counts the  $v_x$  of all molecules staying in the space of a statistical layer, so it can be named the spatial  $v_x$  distribution to distinguish from the flux  $v_x$  distribution. The longer the molecules stay in a statistical layer, the more times they will be recorded in the spatial distribution. Even if there is no collision, the molecular velocity may be repeatedly recorded in the spatial distribution. Therefore, the statistical method based on the molecular flux is more convenient for observing the  $v_x$  distribution after collisions.

The blue dotted line in Fig. 11 represents the result of flux  $v_x$  distribution at the interface featured with  $K_{\min}$ , and this interface is denoted as the  $K_{\min}$  interface. Figure 11(a) shows that in case 6.1, the flux  $v_x$  distribution at interface  $z = 0.1\lambda_0$  (see the red long dashed line) is still the reflected molecular peak at  $v_x/a_0 = 0$ . The flux  $v_x$  distribution at interface  $z = 3\lambda_0$  (see the green short dashed line) is the superposition of a reflected molecular peak and a platform-shaped distribution, which means that some reflected molecules have undergone dual-wall molecular collisions. Because in case 6.1,  $\beta = 0$  (i.e.,  $\beta_0 = \beta_1 = 0$ ), a molecule will only occur one dual-wall molecular collision between two successive reflections. Then, after all the molecules reflected from the lower wall have already collided once, their flux  $v_x$  distribution will remain the platform-shaped distribution in their subsequent motion. It can be seen that the flux  $v_x$  distribution at interface  $z = 5.5\lambda_0$  almost coincides with that at the upper wall ( $z = 6\lambda_0$ ), and their  $K(v)$  both approximate  $K_{\min}$  ( $= 1.81$ ) with deviations less than  $10^{-2}$ . Thus, the interface  $z = 5.5\lambda_0$  is selected as the  $K_{\min}$  interface with a typical platform-shaped distribution. As shown in Figs. 11(b), when  $\beta_0 = 1$ , re-collisions will occur, and the increased number of collisions will lead to further relaxation. Hence, the flux  $v_x$  distribution at the  $K_{\min}$  interface deviates from the typical platform-shaped distribution and transforms into an ordinary unimodal structure with  $K_{\min} = 2.20$ . When  $\beta_1 = 1$ , the same-wall molecular collision will happen. However, the result shown in Fig. 11(c) [or 11(d)] is only slightly different from that shown in Fig. 11(a) [or 11(b)]. The results shown in Fig. 11 confirm the conclusions in Sec. III.A, i.e.,  $v_x$  is uniformly distributed after the dual-wall molecular collision, the same-wall molecular collision has little effect on the  $v_x$  distribution, and the  $v_x$  distribution after the non-dual-wall molecular collision is nonuniform.

Figure 12 compares the variations of  $v_x$  distribution in the cases with different  $\beta$  ( $= 0, 0.2, 0.5, \text{ and } 1$ ) based on the two statistical ways. Compared with Fig. 11, Figs. 12(a-d) show the more detailed variation of flux  $v_x$  distributions at representative interfaces (especially the  $K_{\min}$  interface) caused by the increase of  $\beta$ . Figures 12(e-h) show that spatial  $v_x$  distributions in the  $K_{\min}$  layer (see blue dotted lines) and other representative statistical layers gradually change with  $\beta$ . For case 6.1 with  $\beta = 0$ , Fig. 12(e) also shows that the spatial  $v_x$  distribution near the upper wall [its  $K(v) = 1.60$ ] has two peaks at abscissas  $v_x = 0$  and  $u_{\text{up}}$ , but they are not reflected molecular peaks. This is because, referring to Fig. 12(a), the reflected molecules have already occurred the dual-wall molecular collision once. Thus, the two peaks are formed by the relaxed molecules with  $v_x$  close to 0 and  $u_{\text{up}}$ , respectively. This distribution is owing to the central collision. According to Eq. (3), if the collision angle ( $\theta$ ) is 0 (i.e., the central collision), the  $v_x$  after the collision will equal 0 or  $u_{\text{up}}$ . Two molecules after the central collision will exchange their molecular velocities ( $v$ ) but not change their  $v$  distribution. Hence, the central-collision molecules will preserve the wall velocity information and have a relatively small  $|v_z|$ . For the molecule passing through any equidistant statistical layer (with the constant spacing of  $0.1\lambda_0$ ), its travelling time is proportional to  $1/|v_z|$ . Then, the smaller its  $|v_z|$  is, the longer it travels through this layer, and the more times its  $v_x$  will be recorded in the spatial  $v_x$  distribution in this layer. Therefore, compared with the molecules after eccentric collisions, central-collision molecules will stay in the statistical layer for a longer time and be counted repeatedly to form the bimodal peaks. Qualitatively, this bimodal phenomenon is still similar to the result

in case 2.1 [see Fig. 6(a)], i.e., the wall velocity information cannot be fully relaxed by very few collisions. As  $\beta$  and  $N_{\text{total}}$  increase, the further relaxation will cut the two peak values down and eliminate the wall velocity information, and the spatial  $v_x$  distribution transforms into the platform-shaped distribution [see Fig. 6(h), its  $K_{\text{min}} = 2.03$ ]. Therefore, although the non-dual-wall molecular collision is not the root cause of the platform-like phenomenon, it still plays an important role in the equivalent relaxation process that generates the platform-shaped spatial  $v_x$  distribution.

Figures 12(a-d) show that when  $\beta$  increases, the  $K_{\text{min}}$  interface gradually approaches the lower wall (i.e., from  $L_{K_m} = 5.5\lambda_0$  to  $4.8\lambda_0$ ). A similar trend of the  $K_{\text{min}}$  layer (i.e., from  $L_{K_m} = 5.8\lambda_0$  to  $4.4\lambda_0$ ) can also be seen in Figs. 12(e-h). This trend is mainly because the increased non-dual-wall molecular collisions accelerate the relaxation of wall velocity information. In the flow with  $\beta = 0$ , the reflected molecule after the dual-wall molecular collision is deemed the relaxed molecule and no longer collides. Thus, for the molecules reflected from a certain wall, their number will be continuously reduced by dual-wall molecular collisions when they fly away from this wall. Then, the further these reflected molecules fly away from this wall, the fewer their number remains, and the less chance the residual reflected molecules collide, which will slow down the relaxation of wall velocity information. From the perspective of symmetry, moving away from this wall also means approaching the opposite wall, so the relaxation rates near both walls are relatively low. However, in the flow with  $\beta \neq 0$ , the relaxed molecules may re-collide with reflected molecules, which increases the likelihood and number of collisions of all molecules. Therefore, with the increase of  $\beta$ , the more the collisions occur, the shorter the distance of reflected molecules relaxing from the wall to the relaxation state featured with  $K_{\text{min}}$  is.

In order to explore the influence of flow parameters on the dual-wall molecular collision, Table 7 gives the settings of flow cases with  $\beta = 0$  in group 7.

Table 7  
Settings of group 7.

Group 7	$L_z/\lambda_0$	$u_{\text{up}}/a_0$	$\gamma\lambda_0/a_0$	$T_w(\text{K})$	$\alpha$	$\beta$
Case 7.1	10	6	0.600	300	1	0.0
Case 7.2	8	9	1.125	300	1	0.0
Case 7.3	6	12	2.000	300	1	0.0
Case 7.4	6	15	2.500	300	1	0.0

Figure 13 shows the flux  $v_x$  distributions at the  $K_{\text{min}}$  interfaces in group 7. The simulation results of the flows with  $\beta = 1$  in Sec. II.B indicate that the larger  $\gamma\lambda_0/a_0$  is, the more typical the platform-shaped distribution is. If  $\gamma$  is small, the flow is close to the quasi-equilibrium flow, e.g., case 1.2 shown in Fig. 5(b). As shown in Fig. 7, if  $\gamma$  is large enough, there is still a platform-shaped distribution even in case 3.1 with a relatively small  $u_{\text{up}}$ . However, according to the inference in Sec. III.A, the  $v_x$  distribution after the dual-wall

molecular collisions is only determined by  $c_r (\approx u_{up})$  and is independent of  $\gamma$ . Thus,  $\gamma$  is meaningless in the flow with  $\beta=0$ . For example, in case 7.1 with a small  $\gamma$ , there is still a platform-shaped distribution. Then, the variation of the flux  $v_x$  distribution at the  $K_{min}$  interface (see Fig. 13) mainly reflects the influence of  $u_{up}$ . It can be seen that with the increase of  $u_{up}$ ,  $L_{Km}$  decreases from  $z=9.6\lambda_0$  (case 7.1) to  $5.5\lambda_0$  (case 7.4). This is because in the flows of group 7, the thermal velocity of reflected molecules ( $v_{Tw}$ ) based on  $T_w$  is relatively small, and the magnitude of  $c_r$  is mainly determined by  $u_{up}$ . Then, according to the VHS model, for the dual-wall molecular collisions ignoring  $v_{Tw}$ , their collision cross-sections are roughly correlated with  $u_{up}^{1-2\omega} (= u_{up}^{-0.62})$ , and their  $P_{dual}$  are correlated with the velocity (i.e.,  $u_{up}$ ) that they swept, that is, proportional to  $u_{up} \times u_{up}^{1-2\omega} = u_{up}^{0.38}$ . Hence, within a  $\Delta t$ , the higher  $u_{up}$  is, the larger the space swept by upper-wall-reflected molecules are, the more likely the dual-wall molecular collisions happen, and the shorter  $L_{Km}$  is. This also explains the corresponding settings of  $L_z$  (from  $10\lambda_0$  to  $6\lambda_0$ ) in group 7, i.e., to ensure that all reflected molecules can experience one dual-wall molecular collision to obtain a typical platform-shaped distribution. The  $K_{min}$  value changes from 2.05 (case 7.1) to 1.81 (case 7.4), which indicates that as  $u_{up}$  increases, the flow is getting closer to the hypothetical flow mentioned in Sec. III.A (i.e.,  $v_T$  is far less than  $u_{up}$ ), and the platform-shaped distribution approaches the standard uniform distribution too.

The decoupling study based on taking the dual-wall molecular collision as an independent factor shows that  $u_{up}$  and  $c_r$  will affect  $L_{Km}$ , which partly explains why the  $L_{Km}$  of group 3 cases in Fig. 7 is not linearly with  $\lambda$ . It should be pointed out that the non-dual-wall molecular collision also plays a part in the strong shear nonequilibrium. However, we cannot decouple the non-dual-wall molecular collision from the dual-wall molecular collision in the simulation of strong shear flow, because the dual-wall molecular collision is the physical root of strong shear nonequilibrium. Thus, as mentioned in the discussion of group 3 cases, for any flow case with a platform-like phenomenon, the total effect of all collisions leading to the platform-like phenomenon can be qualitatively regarded as an equivalent relaxation process. This analogy may not be accurate enough, but it will help us analyze and understand the strong shear relaxation process in more general flows in Sec. IV.

In summary, the flux distribution reflects the speed information of the last collision of molecules before passing through an interface. Because the distribution of  $v_x$  after the dual-wall molecular collision is uniform, there is a typical platform-shaped flux  $v_x$  distribution at the  $K_{min}$  interface in case 6.1 with  $\beta=0$ . The spatial distribution reflects the ensemble average speed information of molecules existing in a statistical layer. The spatial  $v_x$  distribution in the  $K_{min}$  layer of case 6.1 is nonuniform due to the weighting relation shown in Eq. (7). This non-uniformity can be further relaxed and eliminated by more collisions, so a platform-shaped spatial  $v_x$  distribution is shown in case 6.3 with  $\beta=1$ . In Fig. 12, the dominant factor of all platform-like phenomena based on different statistical ways is the dual-wall molecular collision. In Fig. 2, the global-space distribution is the superposition of two half-space distributions that are correlatively symmetrical to each other. Hence, the physical root of the platform-like transition [see Fig. 2(a)] is still the dual-wall molecular collision.

In the flow with  $\beta = 0$ , the wall velocity information is continuously relaxed by dual-wall molecular collisions while diffusing along the  $z$  direction. The platform-shaped distribution will appear when almost all reflected molecules have experienced one dual-wall molecular collision. Therefore, the position of the platform-like phenomenon can flag the relaxation distance of the wall velocity information relaxing to a specific state. However, the non-dual-wall molecular collision also plays an important role in the relaxation process in the flow with  $\beta \neq 0$ . Because it is difficult to exclude the dual-wall molecular collision and study the effect of non-dual-wall molecular collision alone, we can only analyze the equivalent relaxation process causing the platform-like phenomenon by analogy with the relaxation of the dual-wall molecular collision.

Someone may wonder whether the platform-like phenomenon is caused by the simplified modelling of intermolecular interaction (i.e., the VHS collision model) in DSMC. In fact, the appendix shows that the platform-shaped distribution also exists in the MD result.

## 4 Extend Cases Of General Flows

The results and conclusions in Sec. III are based on a hypothetical Couette flow, but the symmetry of Couette flow is not common in general flows. We are more interested in whether the specific relaxation phenomenon found in this study can be used as a reference for more general strong shear flow. The hypersonic rarefied argon gas flow over a flat plate was selected to model a more common situation. Most DSMC settings remain the same in Sec. II.A. The computational domain (see Fig. 14) is  $1.2 \text{ m} \times 0.8 \text{ m}$  ( $x \times z$ ). The length of the plate is  $L_x = 1.1 \text{ m}$ . The coordinate origin is located at the left end of the plate. The boundary condition of gas is the freestream with  $n_\infty = 1.333 \times 10^{20} \text{ m}^{-3}$ ,  $T_\infty = 300 \text{ K}$ ,  $a_\infty = 322.6 \text{ m/s}$ , and  $\lambda_\infty = 10 \text{ mm}$ . The streamwise direction is the positive  $x$  direction.  $T_w$  remains  $300 \text{ K}$ , and gas molecules are diffusely reflected on the wall, i.e.,  $\alpha = 1$ . The near-wall cell sizes were still refined to be  $\lambda_\infty/10$  ( $= 1 \text{ mm}$ ). Two flow cases with different freestream velocities ( $u_\infty = 4840$  or  $1936 \text{ m/s}$ , i.e.,  $Ma_\infty = 15$  or  $6$ ) were simulated.

The contours of equivalent temperature ( $T_e$ ) and translational velocity ( $u_x$ ) of the flow at  $Ma_\infty = 15$  are shown in Fig. 14. It can be seen that near the wall, there are wedge-like regions with large  $z$ -direction gradients of  $T_e$  and  $u_x$ . This is because the reflected molecules carrying wall velocity information not only spread along the  $z$  direction, but also be driven by freestream in the  $x$  direction. Thus, the resultant motion of reflected molecules in the two directions forms a wedge-like region strongly affected by the wall. Figure 14(a) shows that within the area  $z < 100 \text{ mm}$ , there is an aerodynamic heating layer whose  $T_e$  is conspicuously higher than that on the upper and lower sides. Meanwhile, among all cells at a given  $x$  coordinate, the cell with  $K_{\min}$  [see the red dot in Fig. 14(a)] is just located in this heating layer. It can be seen that the height of the  $K_{\min}$  cell (i.e.,  $L_{K_{\min}}$ ) increases along the streamwise direction. The cells with  $S_0$  [see dark squares in Fig. 14(a)] are a bit higher ( $< 4 \text{ mm}$ ) than the  $K_{\min}$  cells. Even though the  $S_0$  cells do not coincide with the  $K_{\min}$  cells in this asymmetric flow, their positions are still very close. Thus, like the

result in Sec. 2, i.e., the most significant nonequilibrium phenomenon occurs in the  $K_{\min}$  layer, there may be some strong nonequilibrium in the  $K_{\min}$  cell in this flat-plate flow.

Figure 14(b) shows that the variation of  $u_x$  contour is mainly concentrated in the region below isoline  $u_x = 4000$  m/s, and this region expands linearly along the  $x$  direction, so the near-wall  $y$  decreases accordingly. This situation is somewhat similar to the flowfield settings in cases of group 2 in Sec. 2.3.2, i.e., the height (denoted as  $H_z$ ) from the wall to the position with a fixed translational velocity (e.g., isoline  $u_x = 4000$  m/s) is variable. More specifically, we take all cells at a given  $x$  coordinate below isoline  $u_x = 4000$  m/s as a separate flowfield segment, and assume that the change of  $v_x$  distribution in this segment is equivalent to the relaxation process in an imaginary flow. Then,  $H_z$  is the total relaxation distance in this imaginary process, which is similar to the role  $L_z$  in Couette flow. As shown in Fig. 14(a),  $L_{K_m}$  of the imaginary flow increases with  $H_z$ , which is just like the trend of  $L_{K_m}$  varying with  $L_z$  in group 2 (see Fig. 6). The variation of  $v_x$  distribution can show more similarities between the two flow situations. Figure 15 shows the global-space  $v_x$  distributions of the flow at  $Ma_\infty = 15$  in the cell  $z = 1$  mm (see red dashed lines), the  $K_{\min}$  cell (see blue dotted lines), and cell  $u_x = 4000$  m/s (see dark solid lines) at three representative  $x$  coordinates ( $= 0.15, 0.55, \text{ and } 0.95$  m).

For a certain cell in the flow over a flat plate, its  $v_x$  distribution mainly reflects the flowfield information from the upstream dependent domain. Hence, the change of  $v_x$  distribution in a flow segment is not an actual relaxation process but an imaginary one. However, although not identical, the change rule of  $v_x$  distribution shown in Fig. 15 can be explained by analogy and referring to some similar features of  $v_x$  distribution in the flows of group 2. For example, the  $v_x$  distribution in the  $K_{\min}$  cell in Fig. 15 shows a change similar to that in the  $K_{\min}$  layer in Fig. 6, i.e., with the increase of total relaxation distance, the curve of  $v_x$  distribution transforms from a bimodal structure into a platform-like structure and finally into an ordinary unimodal structure. As shown in Fig. 15(a), at  $x = 0.15$  m,  $H_z = 22$  mm, and  $L_{K_m} = 9$  mm. At this position, the length of the flat plate through which the freestream flows is short, and the reflected molecules have not accumulated too much near the wall, so freestream molecules only experienced very few collisions with reflected molecules. Thus, the wall velocity information will not be fully relaxed within such a short  $L_{K_m}$ , but a bimodal structure including the reflected molecular peak and the freestream molecular peak is formed in the  $K_{\min}$  cell, which is similar to the result of case 2.1 [see Fig. 6(a)]. As shown in Fig. 15(b),  $H_z$  rises to 76 mm at  $x = 0.55$  m. Similar to the result of case 2.3 [see Fig. 6(c)], when the relaxation distance is long enough to relax and eliminate the wall velocity information completely, a platform-shaped  $v_x$  distribution appears in the  $K_{\min}$  cell at  $z = 29$  mm. At  $x = 0.95$  m, the bulk flow has travelled a long distance along the wall, and a large number of low-speed molecules have accumulated near the wall. As shown in Fig. 15(c),  $H_z$  rises to 130 mm ( $> 10\lambda_\infty$ ) and exceeds the traditionally considered range of the Knudsen layer. The upstream molecules have already collided many times. They have been relaxed to some extent. Their  $v_x$  distribution forms an ordinary unimodal structure like the distribution shown in Fig. 6(e). Figure 15 shows that the equivalent relaxation process leading to the

platform-like phenomenon exists in the flow over a flat plate, which implies that in more general flow, there should be a physical mechanism similar to the dual-wall molecular collision. Considering that the freestream molecules have small thermal velocity and large translational velocity, which is similar to the features of upper-wall reflected molecules in the hypothetical Couette flow, it is obvious that the first collision of the reflected molecule with the freestream molecule is just such a similar mechanism.

Figure 16 shows the contours of  $T_e$  and  $u_x$  of the flow at  $Ma_\infty = 6$ . This flow also has a wedge-like region, but its  $T_e$  and  $u_x$  gradients are not as intense as those in the flow at  $Ma_\infty = 15$ . The  $K_{\min}$  cell and  $S_0$  cell are also roughly located in the heating layer, and the violent gradient changes of  $T_e$  and  $u_x$  are still concentrated near the wall.

Figure 17 shows the global-space  $v_x$  distributions of the flow at  $Ma_\infty = 6$  in the cell  $z = 1$  mm (see red dashed lines), the  $K_{\min}$  cell (see blue dotted lines), and the cell  $u_x = 1500$  m/s (see dark solid lines) at  $x = 0.15, 0.25,$  and  $0.55$  m. It can be seen that there is a platform-shaped distribution in the  $K_{\min}$  cell at  $x = 0.15$  m, which somehow recurs the results of case 3.1, i.e., the equivalent relaxation process causing the platform-like phenomenon also occurs in a more general flow with short relaxation distance, large  $\gamma$  but small  $u_\infty$ . Compared with the platform-like phenomenon in the flow at  $Ma_\infty = 15$  [see Fig. 15(b)], the platform-like phenomenon of this flow is closer to the upstream because of its small  $Ma_\infty$  and closer to the wall because of its small  $T_e$ . With the decrease of near-wall  $\gamma$  along the streamwise direction, the  $v_x$  distribution will be further relaxed into a state closer to equilibrium.

## 5 Conclusion

A series of Couette flow cases of rarefied argon gas were simulated by DSMC. In any case with a strong shear, there is always a phenomenon that the maximum variance ( $\sigma_{\max}$ ), zero-value skewness ( $S_0$ ), and minimum kurtosis ( $K_{\min}$ ) of the statistical moment functions of molecular velocity distribution coexist near a certain layer (i.e., the  $K_{\min}$  layer), and these features ( $\sigma_{\max}$ ,  $S_0$ , and  $K_{\min}$ ) are closely related to the strong shear nonequilibrium. Especially in the flow with small wall spacing, large wall speed ( $u_{\text{up}}$ ), and diffuse-reflection walls, the streamwise velocity (i.e.,  $v_x$ ) in  $K_{\min}$  layer presents a qualitative platform-shaped distribution. In the relaxation process with such a platform-like phenomenon, the formation of platform-shaped distribution is accompanied by the elimination of wall velocity information represented by the reflected molecular peak. A similar platform-like phenomenon can also be found in the hypersonic flow over a flat plate, meaning that the platform-shaped distribution is a universal nonequilibrium phenomenon under strong shear.

According to the trend of platform-like phenomenon varying with the flowfield and wall settings, an idealized Couette flow with extreme conditions was conceived to analyze the mechanism of the platform-like phenomenon. Based on this hypothetical flow, it can be proved that for two molecules reflected from different walls, their  $v_x$  will be uniformly distributed after their first collision with each other (i.e., the dual-wall molecular collision). This mechanism is supported by the verification case in which any reflected

molecule will only have one dual-wall molecular collision between two successive reflections. In this flow, the  $v_x$  distribution of molecular flux through the  $K_{\min}$  interface is uniform, and the position of  $K_{\min}$  interface can reflect the influence of shear velocity (e.g.,  $u_{up}$ ) on the relaxation process. The platform-shaped distribution is the specific relaxation state after all wall reflected molecules have collided with the bulk-flow molecules once.

Although the physical root is clear, there are many non-dual-wall molecular collisions in actual flow. They will further relax the velocity distribution after dual-wall molecular collisions and form the platform-like phenomenon within the relaxation distance traditionally regarded as the Knudsen layer (i.e., 1 to 2 local  $\lambda$ ). However, they cannot function independently of the dual-wall molecular collision. We thus can only regard the total effect of all collisions leading to the platform-like phenomenon as some equivalent relaxation process. By analyzing the equivalent relaxation process based on the analogy with the result of the dual-wall molecular collision, we can explain and predict the relaxation phenomenon in a more general hypersonic flow over a flat plate. Therefore, the exploration of the physical mechanism of the platform-like phenomenon in this paper can provide some references for the future modelling research on strong shear Knudsen layer flow.

## Declarations

### Acknowledgements

The authors would like to thank Mr. Zhansen Qian for suggestions about manuscript writing.

### Authors' contributions

The first author was the major contributor to finishing the numerical simulations, and all authors were involved in writing the manuscript. All authors read and approved the final manuscript.

### Funding

This work was supported by the National Key Basic Research Program of China (Grant No. 2014CB744100), China Aerodynamics Research and Development Center, and the high-performance computing (HPC) resources at Beihang University.

### Availability of data and materials

The datasets are available from the corresponding author on reasonable request.

### Competing interests

The authors declare that they have no competing interests.

## References

1. Smoluchowski M (1898) Ueber wärmeleitung in verdünnten gasen. *Ann Phys Chem* 300:101–130
2. Knudsen M (1911) Die molekulare wärmeleitung der gase und der akkommodationskoeffizient. *Ann Phys* 339:593–656
3. Gazizulin RR, Maillet O, Zhou X, Maldonado CA, Bourgeois O, Collin E (2018) Surface-Induced Near-Field Scaling in the Knudsen Layer of a Rarefied Gas. *Phys Rev Let* 120(3):036802
4. Sazhin S (2014) *Droplets and Sprays*. Springer, London, UK
5. Huang Y, Hua X, Shen C, Li F, Mou G (2021) Metal evaporation flux across knudsen layer in laser keyhole welding of Al-Mg alloys with pressure balance condition method. *Appl Surf Sci* 536:147838
6. Ikeda A, Matsumoto M, Ogura S, Okano T, Fukutani K (2013) Knudsen layer formation in laser induced thermal desorption. *J Chem Phys* 138(12):124705
7. Peng Z, Liu S, Li Y, Deng Z, Feng H (2020) Pore-scale lattice boltzmann simulation of gas diffusion-adsorption kinetics considering adsorption-induced diffusivity change. *Energies* 13(18):4927
8. Zhang JB, Li XW, Hang YH, Yang WH (2018) An electrothermal plasma model considering polyethylene and copper ablation based on ignition experiment. *J Phys D Appl Phys* 51(23):235204
9. Rezaei F, Beheshtipour S, Sedeh AB (2020) Truncation of a nanosecond CO<sub>2</sub> laser pulse by following of the temporal characteristics of the plasma parameters in laser ablation model. *Phys Plasmas* 27(6)
10. Bhagat A, Gijare H, Dongari N (2019) Modeling of Knudsen Layer Effects in the Micro-Scale Backward-Facing Step in the Slip Flow Regime. *Micromachines* 10(2):118
11. Norouzi A, Esfahani JA (2015) Two relaxation time lattice Boltzmann equation for high Knudsen number flows using wall function approach. *Microfluid Nanofluid* 18(2):323–332
12. Wang P, Su W, Wu L (2020) Thermal transpiration in molecular gas. *Phys Fluids* 32(8):082005
13. Wang JJ, Kang QJ, Chen L, Rahman SS (2017) Pore-scale lattice Boltzmann simulation of micro-gaseous flow considering surface diffusion effect. *Int J Coal Geol* 169:62–73
14. Gijare H, Bhagat A, Dongari N (2019) Effect of Knudsen Layer on the heat transfer in hypersonic rarefied gas flows. *Int J Therm Sci* 142:134–141
15. Bhagat A, Gijare H, Dongari N (2019) Implementation of Knudsen Layer Phenomena in Rarefied High-Speed Gas Flows. *J Aerosp Eng* 32(6):040191001–040191011
16. Chrusciel GT, Pool LA (1985) Knudsen layer characteristics for a highly cooled blunt body in hypersonic rarefied flow. *AIAA J* 23(6):826–827
17. Ou J, Chen J (2020) Nonlinear transport of rarefied Couette flows from low speed to high speed. *Phys Fluids* 32(11):112021
18. Chen J, Zhou H (2021) Rarefied gas effect in hypersonic shear flows. *Acta Mech Sin* 37(1):2–17
19. Darbandi M, Roohi E (2013) A hybrid DSMC/Navier-Stokes frame to solve mixed rarefied and non-rarefied hypersonic flows over nano-plate and micro-cylinder. *Int J Numer Meth Fluids* 72:937
20. Akhlaghi H, Roohi E (2021) Generalized description of the Knudsen layer thickness in rarefied gas flows. *Phys Fluids* 33(6):061701

21. To QD, Léonard C, Lauriat G (2015) Free-path distribution and Knudsen-layer modeling for gaseous flows in the transition regime. *Phys Rev E* 91(2):023015
22. Whitman JR, Aranovich GL, Donohue MD (2010) Anisotropic mean free path in simulations of fluids traveling down a density gradient. *J Chem Phys* 132(22):224302
23. Dongari N, Zhang YH, Reese JM (2011) Molecular free path distribution in rarefied gases. *J Phys D Appl Phys* 44(12):125502
24. Stops DW (1970) The mean free path of gas molecules in the transition régime. *J Phys D Appl Phys* 3(5):685–696
25. Abramov RV (2017) Diffusive Boltzmann equation, its fluid dynamics, Couette flow and Knudsen layers. *Phys A* 484:532–557
26. Zhang YD, Xu AG, Zhang GC, Chen ZH (2018) Discrete Boltzmann Method with Maxwell-Type Boundary Condition for Slip Flow. *Commun Theor Phys* 69(1):77
27. Abramov RV (2018) Gas near a wall: shortened mean free path, reduced viscosity, and the manifestation of the Knudsen layer in the Navier-Stokes solution of a shear flow. *J Nonlinear Sci* 28(3):833–845
28. Ou J, Chen J (2019) DSMC data-improved numerical simulation of hypersonic flow past a flat plate in near-continuum regime. *Comput Fluids* 194:104308
29. Ejtehadi O, Roohi E, Esfahani JA (2013) Detailed investigation of hydrodynamics and thermal behavior of nano/micro shear driven flow using DSMC. *Sci Iran* 20(4):1228–1240
30. Ou J, Chen J (2020) Hypersonic Aerodynamics of Blunt Plates in Near-Continuum Regime by Improved Navier-Stokes Model. *AIAA J* 58(10):1–10
31. Bhattacharya DK, Lie GC (1991) Nonequilibrium gas flow in the transition regime: A molecular-dynamics study. *Phys Rev A* 43(2):761–767
32. Gu K, Watkins CB, Koplík J (2010) Atomistic hybrid DSMC/NEMD method for nonequilibrium multiscale simulations. *J Comput Phys* 229(5):1381–1400
33. Jiang Y, Gao Z, Jiang C, Lee CH (2017) Hypersonic aeroheating characteristics of leading edges with different nose radii. *J Thermophys Heat Tr* 31:538
34. Liu W, Zhang J, Jiang Y, Chen L, Lee CH (2021) DSMC study of hypersonic rarefied flow using the Cercignani-Lampis-Lord model and a molecular-dynamics-based scattering database. *Phys Fluids* 33(7):072003
35. Yamamoto K, Takeuchi H, Hyakutake T (2006) Characteristics of reflected gas molecules at a solid surface. *Phys Fluids* 18(4):046103
36. Bird GA (1976) *Molecular gas dynamics*. Clarendon Press, Oxford, UK
37. Chen J, Zhao L (2018) A criterion for the existence of local rarefaction effect in a hypersonic flow field and the corresponding flow characteristics. *Acta Aerodyn Sin* 36:4–11 [in chinese]
38. Peddakotla SA, Kammara KK, Kumar R (2019) Molecular dynamics simulation of particle trajectory for the evaluation of surface accommodation coefficients. *Microfluid Nanofluid* 23:79

39. Kovalev V, Yakunchikov A, Li F (2011) Tangential momentum and thermal accommodation coefficients for hydrogen molecules on graphite surface. *Acta Astronaut* 69(7–8):744–746
40. Bentz JA, Tompson RV, Loyalka SK (1997) The spinning rotor gauge: measurements of viscosity, velocity slip coefficients, and tangential momentum accommodation coefficients for  $N_2$  and  $CH_4$ . *Vacuum* 48:817
41. Bentz JA, Tompson RV, Loyalka SK (2001) Measurements of viscosity, velocity slip coefficients, and tangential momentum accommodation coefficients using a modified spinning rotor gauge. *J Vac Sci Tech A* 19:317
42. Tuzun RE, Noid DW, Sumpter BG, Merkle RC (1999) Dynamics of fluid flow inside carbon nanotubes. *Nanotechnology* 7(3):241–246

## Figures

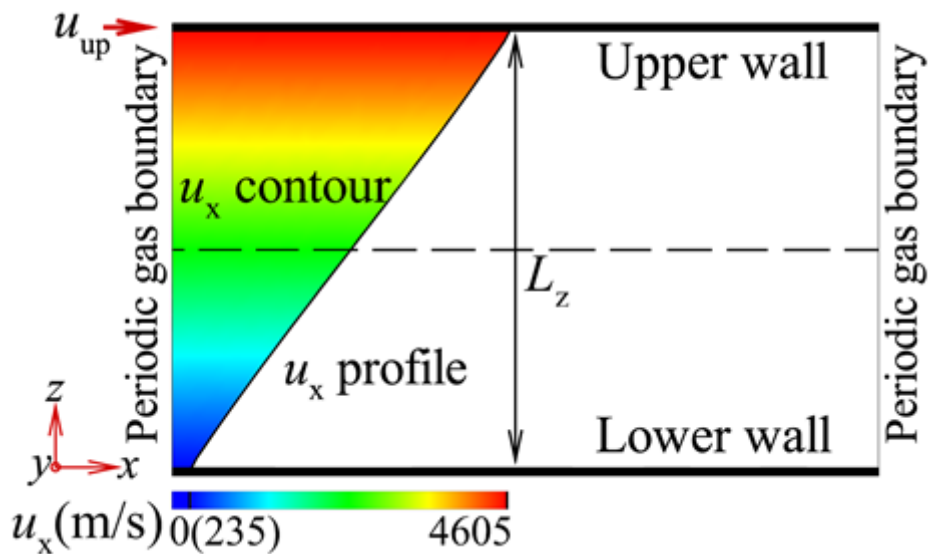
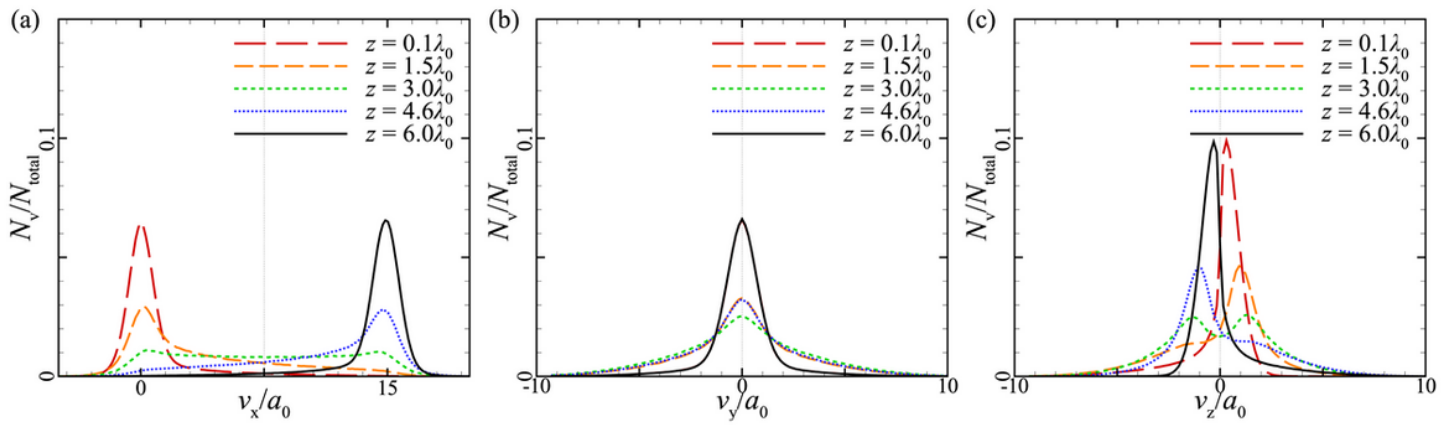


Figure 1

Sketch of plane Couette flow, where  $u_x$  contour is truncated by  $u_x$  profile.



**Figure 2**

Distributions of  $v$  [i.e., variations of  $N_v/N_{\text{total}}$  with  $v_x$  (a),  $v_y$  (b), and  $v_z$  (c)] in different layers (from  $z = 0.1\lambda_0$  to  $6\lambda_0$ ).

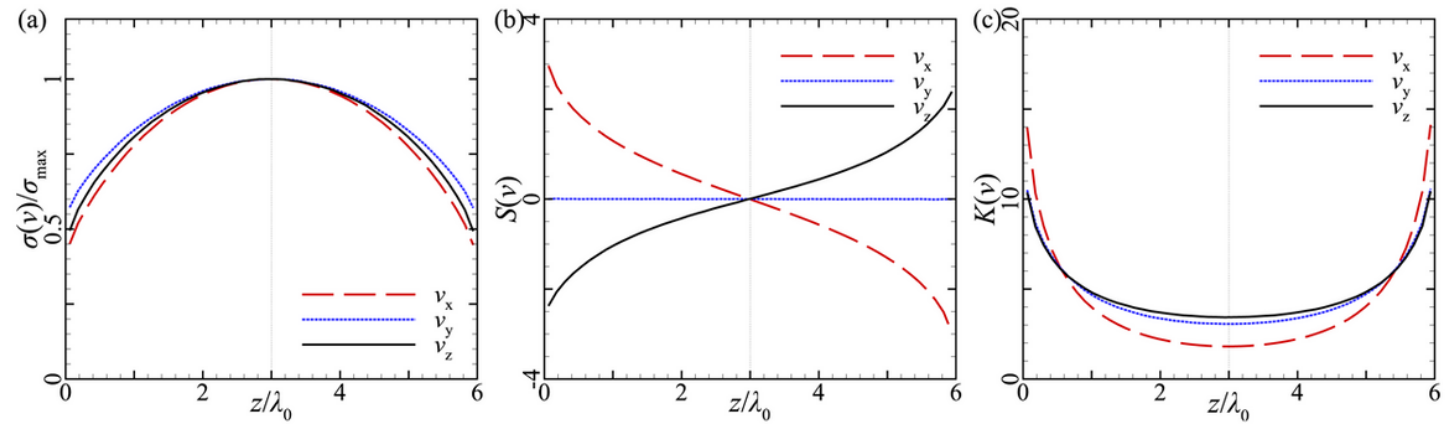


**Figure 3**

Variations of variance  $\sigma(v)/\sigma_{\text{max}}$  (a), skewness  $S(v)$  (b), and kurtosis  $K(v)$  (c) with  $z/\lambda_0$ .

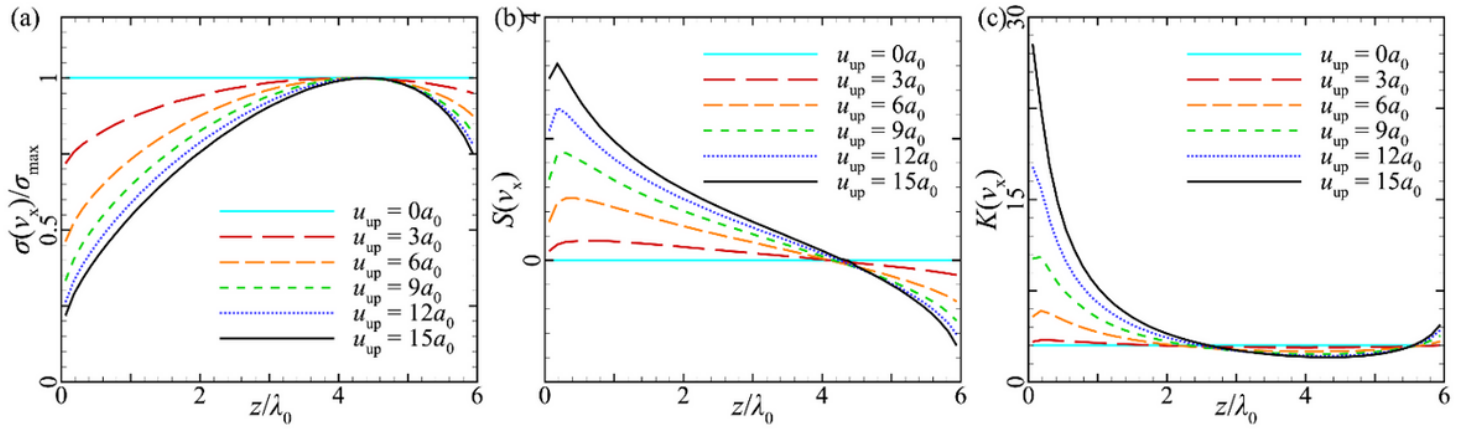


**Figure 4**

Variations of variance  $\sigma(v)/\sigma_{max}$  (a), skewness  $S(v)$  (b), and kurtosis  $K(v)$  (c) with  $z/\lambda_0$  in cases of group 1.

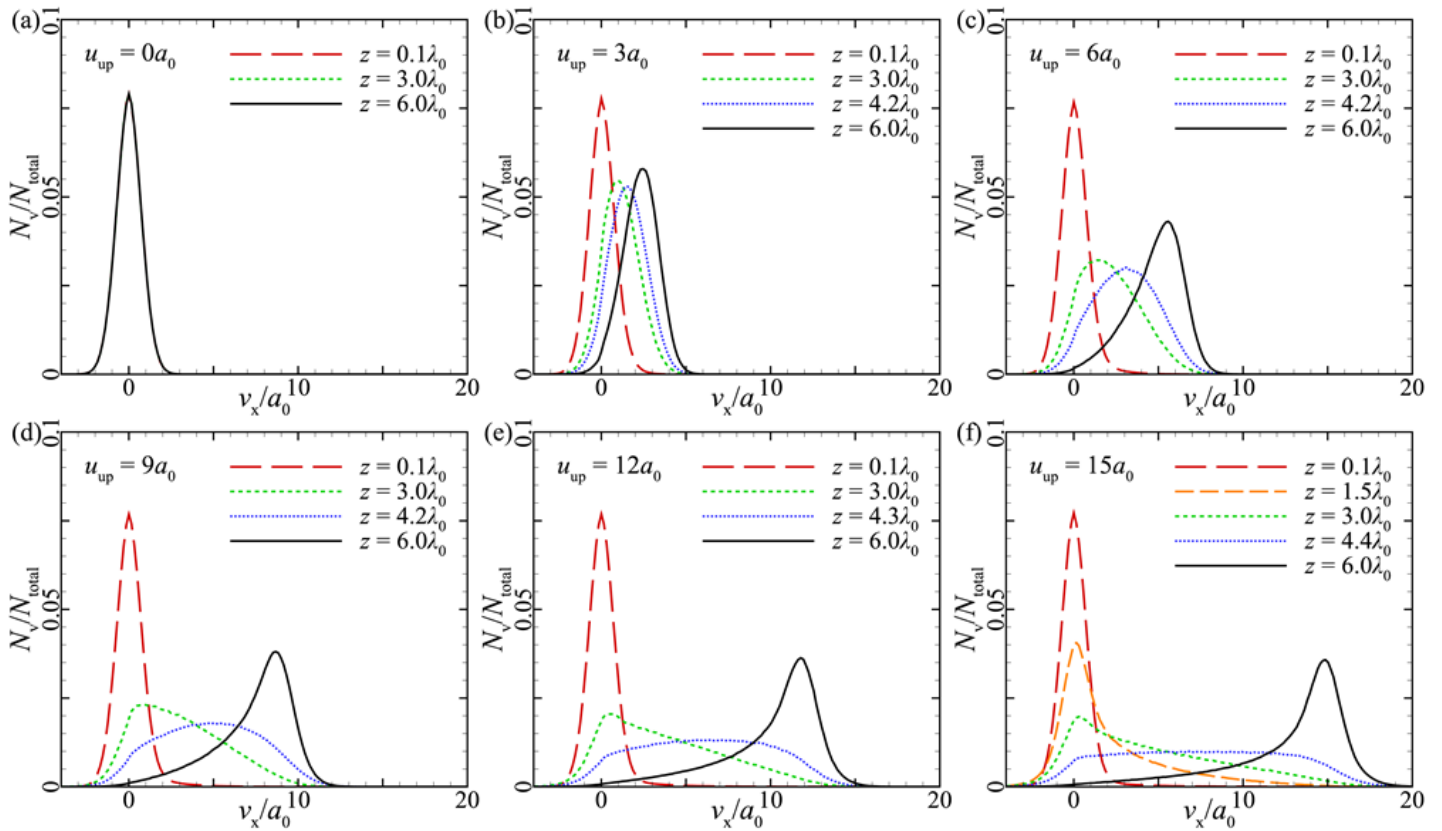


**Figure 5**

Variations of  $v_x$  distributions along the  $z$  direction in cases 1.1-1.6 (a-f).

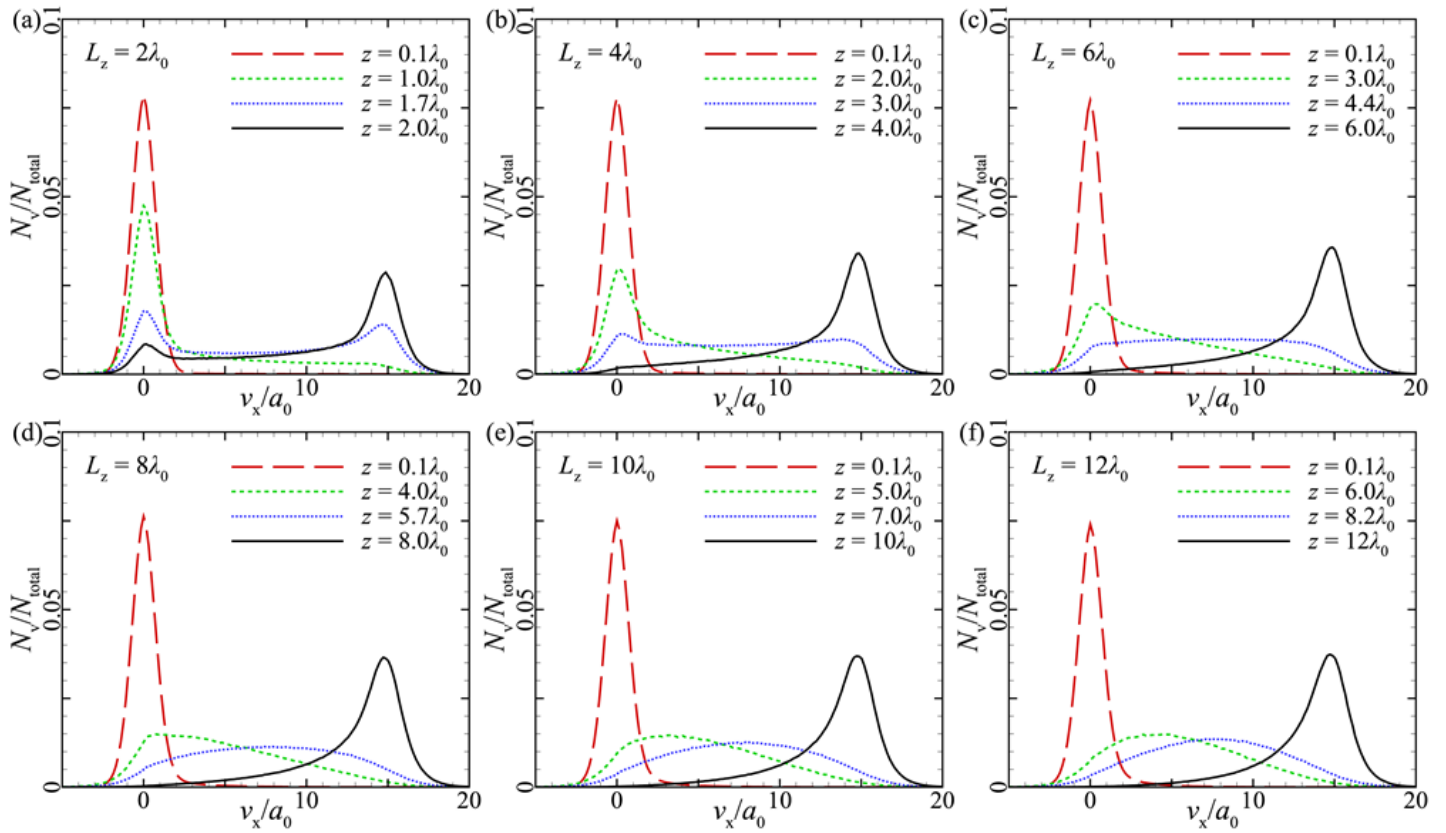


**Figure 6**

Variations of  $v_x$  distributions in cases 2.1-2.6 (a-f).

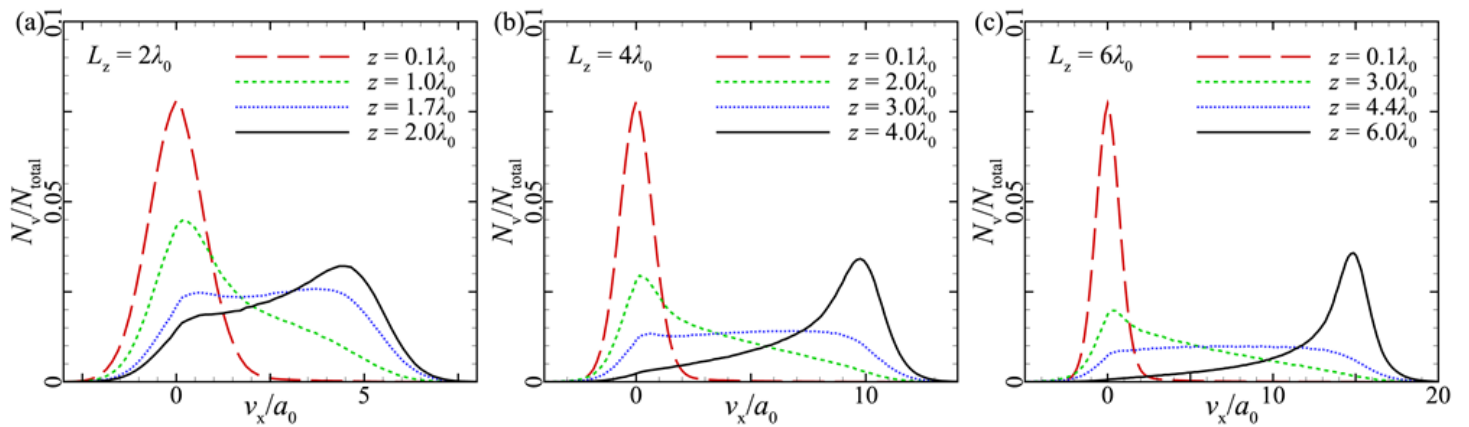


**Figure 7**

Variations of  $v_x$  distributions in cases 3.1-3.3 (a-c).

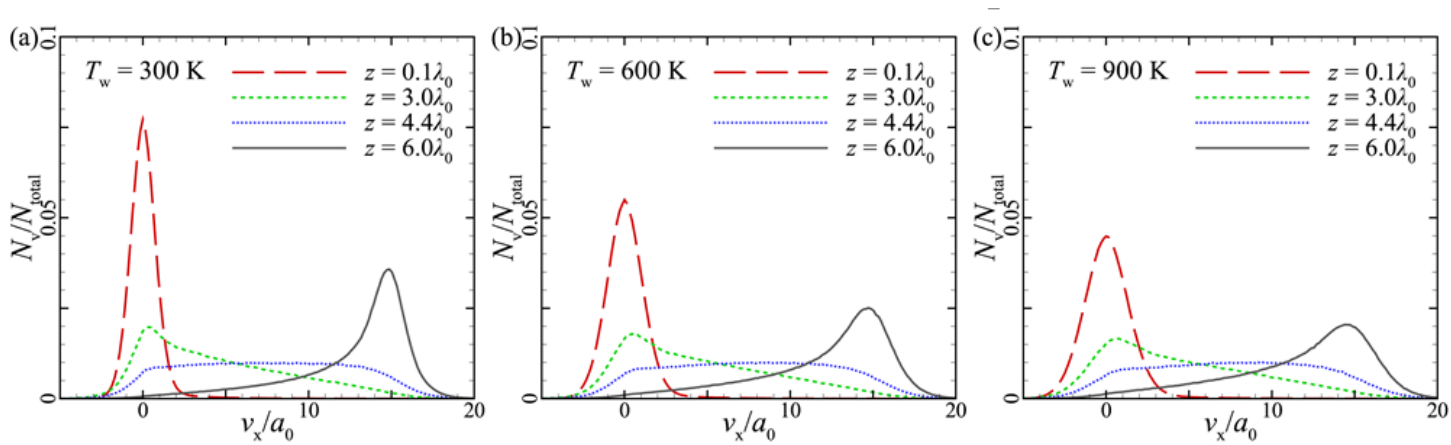


**Figure 8**

Variations of  $v_x$  distributions in cases 4.1-4.3 (a-c).

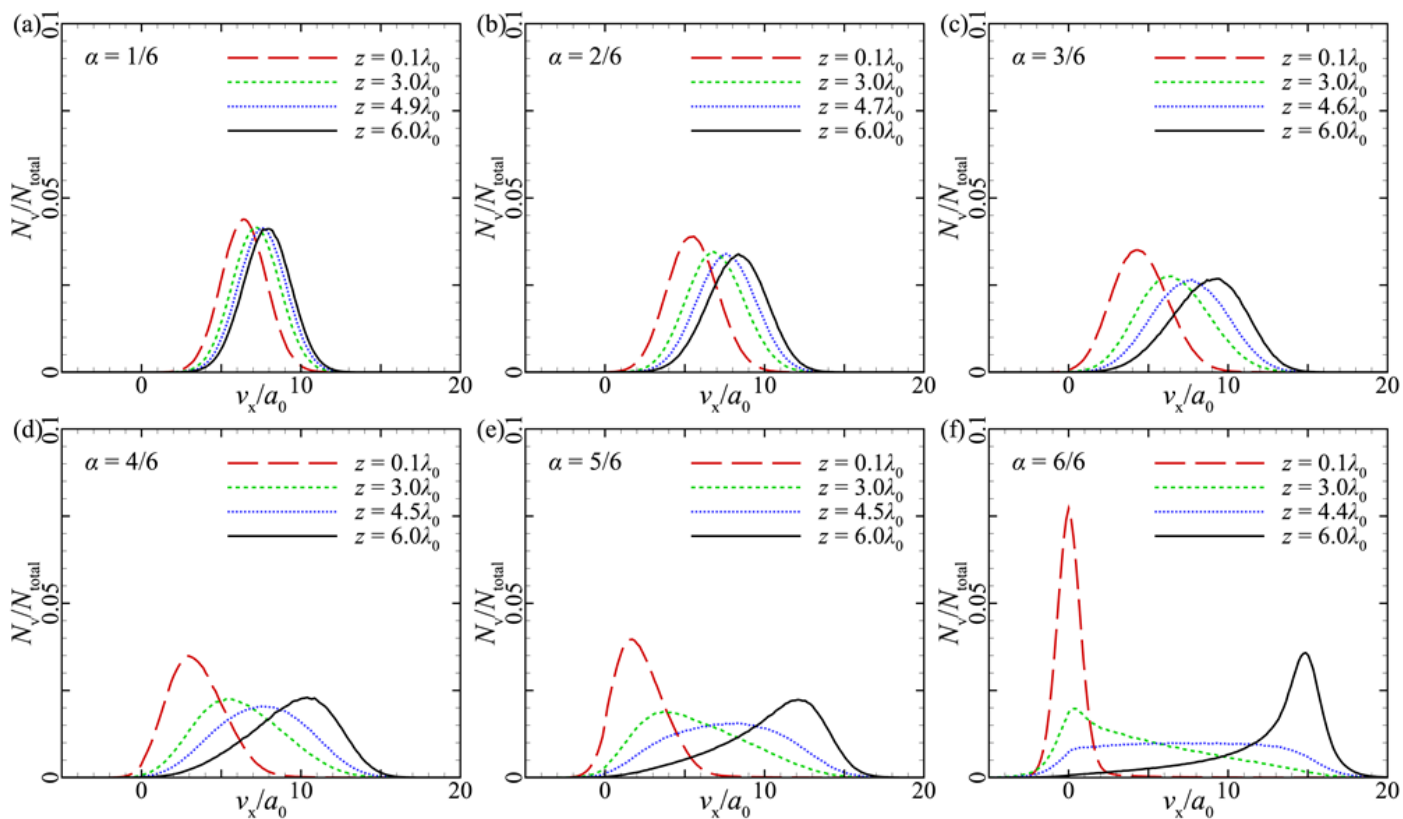


**Figure 9**

Variations of  $v_x$  distributions in cases 5.1-5.6 (a-f).

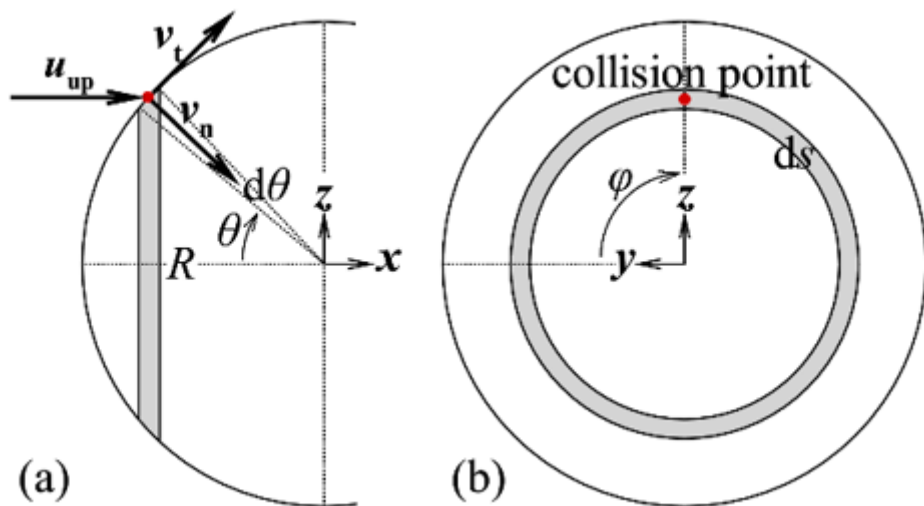


Figure 10

Projections of molecule A on the  $x$ - $z$  plane (a) and  $y$ - $z$  plane (b) in a dual-wall molecular collision.

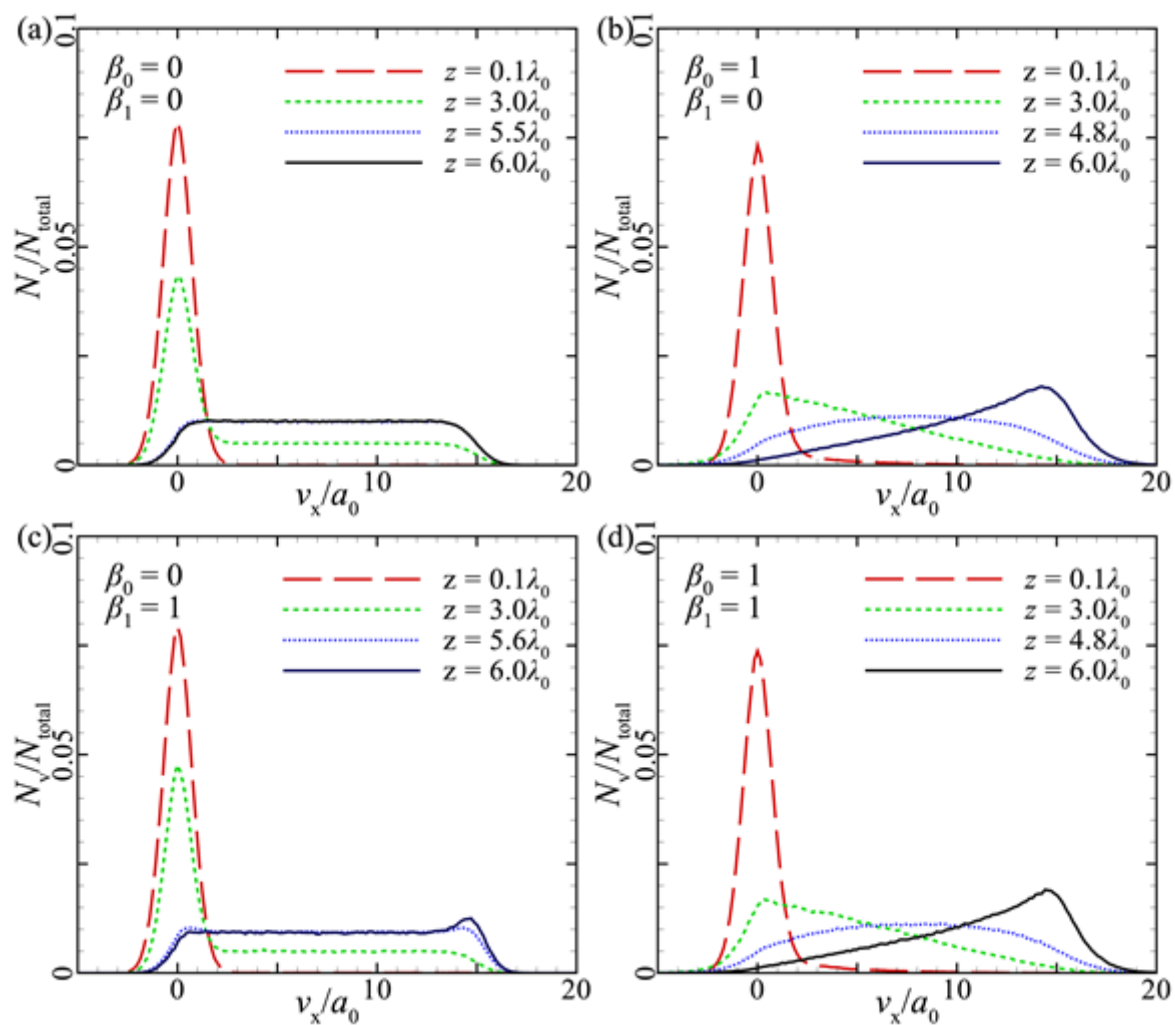


Figure 11

Variations of flux  $v_x$  distributions in cases 6.1-6.4 (a-d).

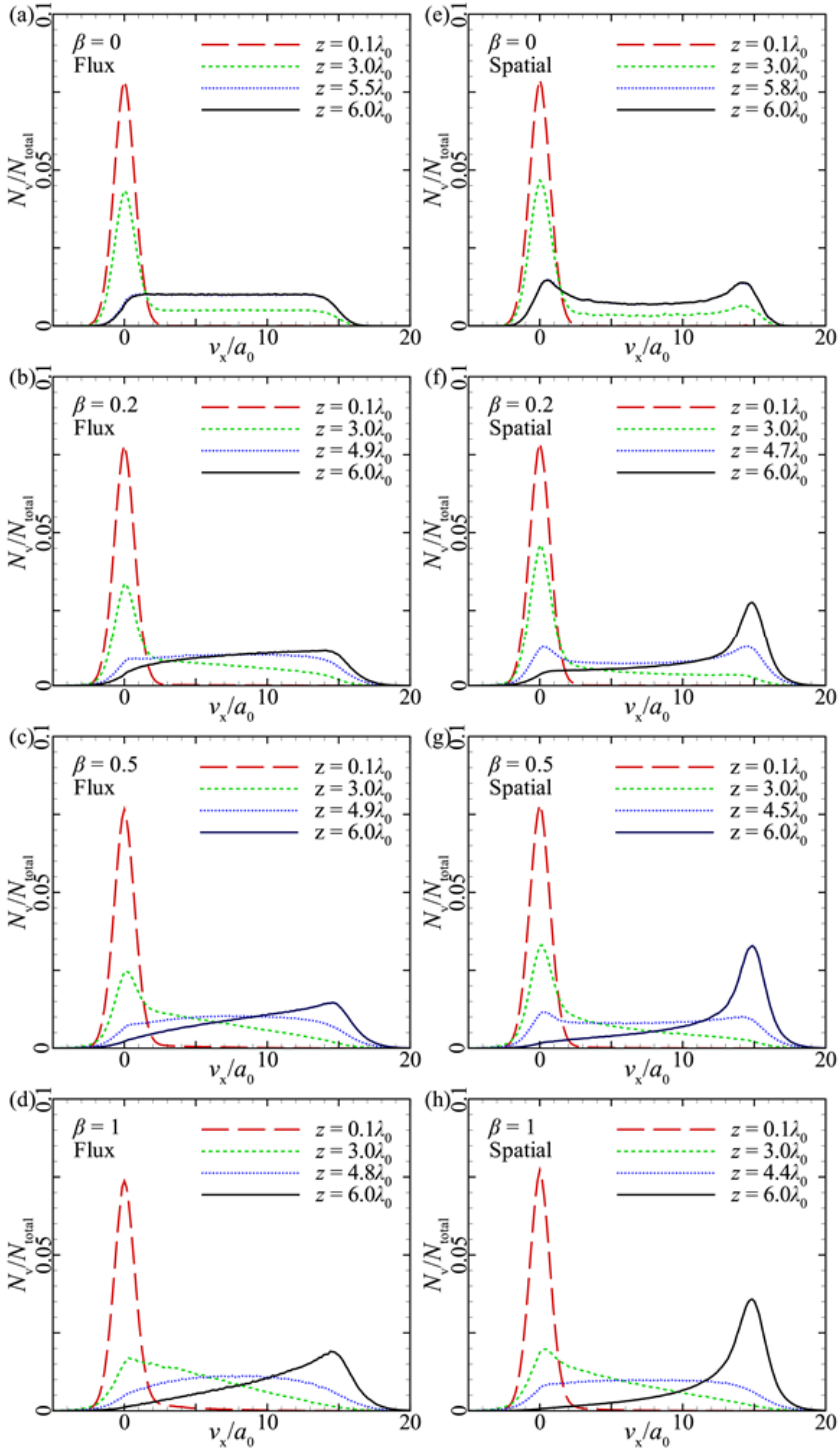


Figure 12

Variations of flux  $v_x$  distributions (a-d) and spatial  $v_x$  distributions (e-h) in cases 6.1(a,e), 6.5(b,f), 6.6(c,g), and 6.4(d,h).

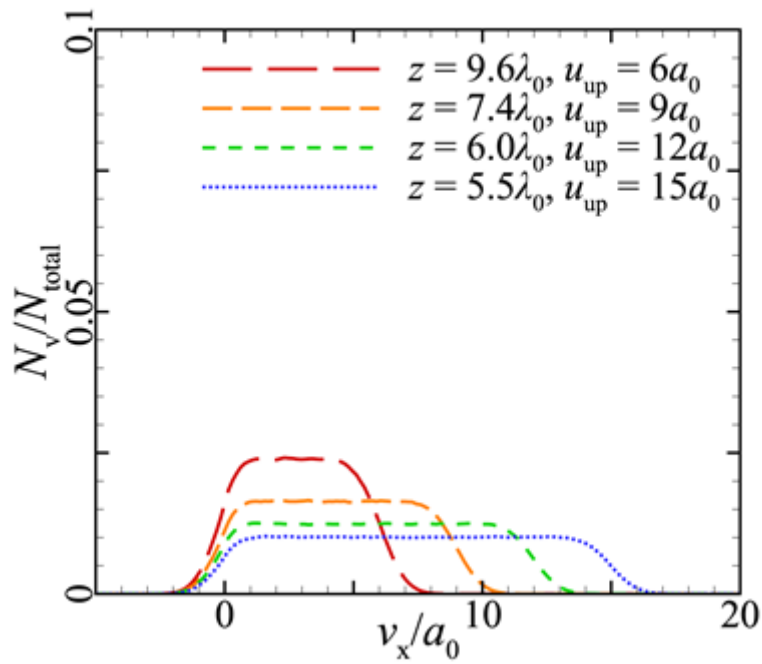


Figure 13

Variation of flux  $v_x$  distributions at the  $K_{\min}$  interfaces with  $u_{\text{up}}$  in group 7.

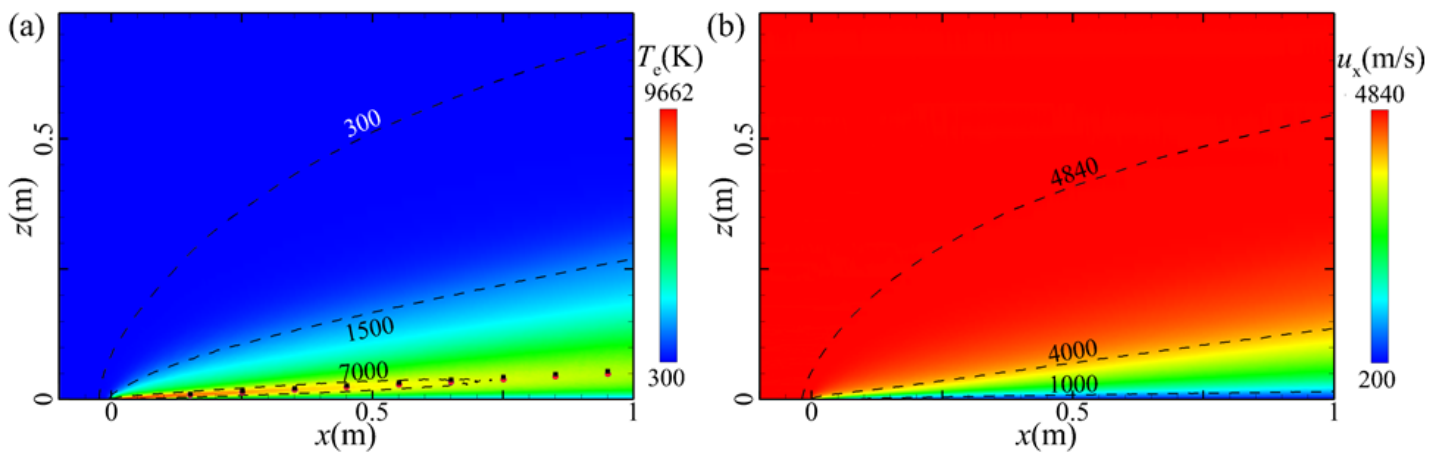
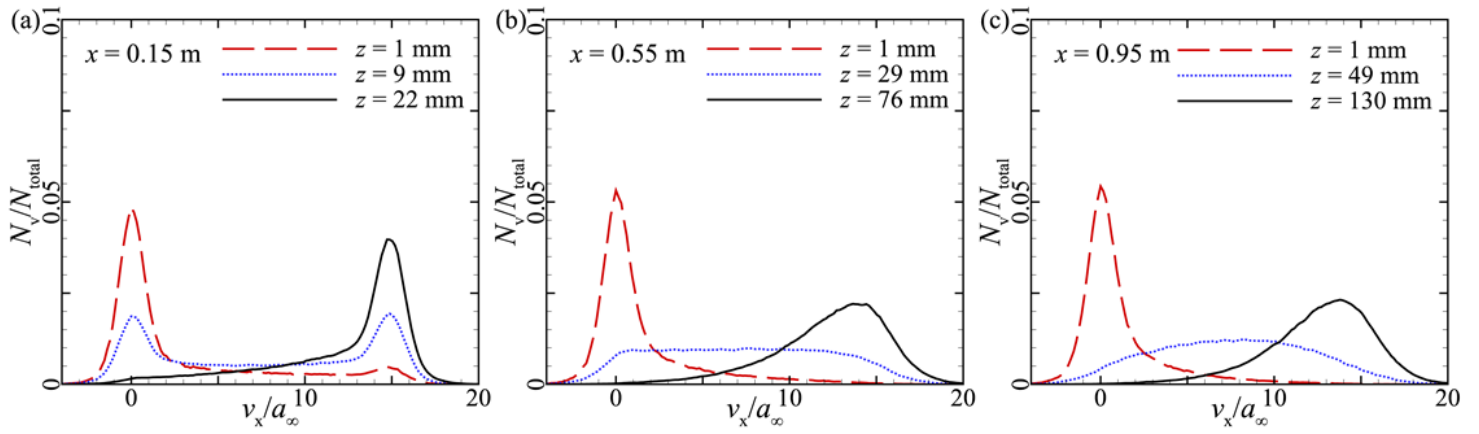


Figure 14

Contours of equivalent temperature  $T_e$  (a) and translational velocity  $u_x$  (b) of the flow at  $Ma_\infty = 15$ .



**Figure 15**

$v_x$  distributions in representative cells at  $x = 0.15$  m (a),  $0.55$  m (b) and  $0.95$  m (c).

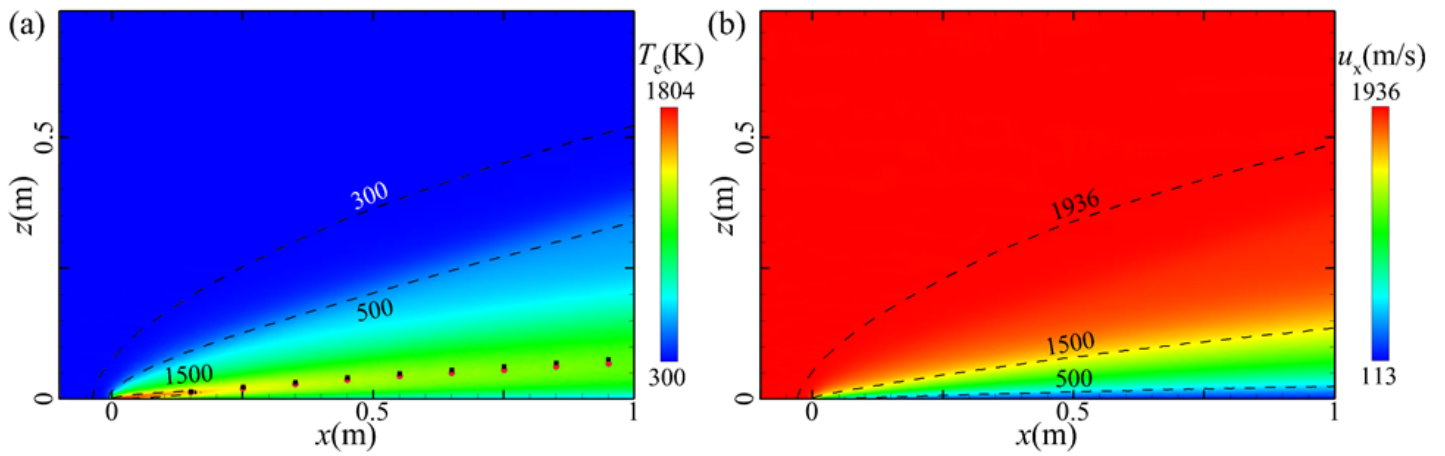


**Figure 16**

Contours of  $T_e$  (a) and  $u_x$  (b) of the flow at  $Ma_\infty = 6$ .

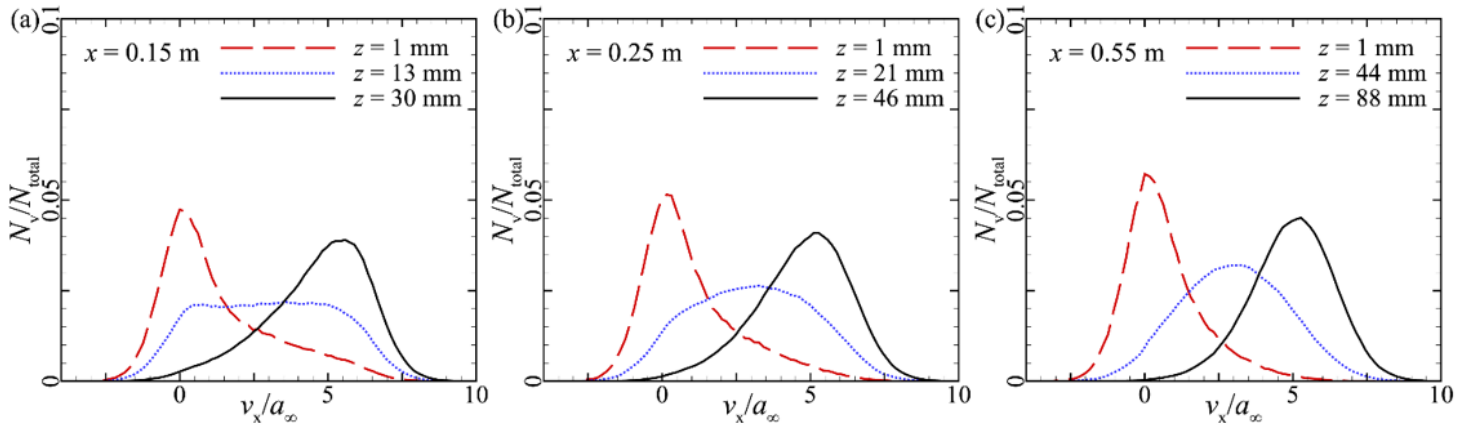


**Figure 17**

Variations of  $v_x$  distributions along the  $z$  direction at  $x = 0.15$  m (a),  $0.25$  m (b) and  $0.55$  m (c).

## Supplementary Files

This is a list of supplementary files associated with this preprint. Click to download.

- [Appendix.docx](#)